Flagellate Underwater Robotics at Macroscale: Design, Modeling, and Characterization

Costanza Armanini [iD], *Associate Member, IEEE*, Madiha Farman, Marcello Calisti [iD], Francesco Giorgio-Serchi [iD], Cesare Stefanini, *Member, IEEE*, and Federico Renda [iD], *Associate Member, IEEE*

Abstract—Prokaryotic flagellum is considered as the only known example of a biological "wheel," a system capable of converting the action of rotary actuator into a continuous propulsive force. For this reason, flagella are an interesting case study in soft robotics and they represent an appealing source of inspiration for the design of underwater robots. A great number of flagellum-inspired devices exists, but these are all characterized by a size ranging in the micrometer scale and mostly realized with rigid materials. Here, we present the design and development of a novel generation of macroscale underwater propellers that draw their inspiration from flagellated organisms. Through a simple rotary actuation and exploiting the capability of the soft material to store energy when interacting with the surrounding fluid, the propellers attain different helical shapes that generate a propulsive thrust. A theoretical model is presented, accurately describing and predicting the kinematic and the propulsive capabilities of the proposed solution. Different experimental trials are presented to validate the accuracy of the model and to investigate the performance of the proposed design. Finally, an underwater robot prototype propelled by four flagellar modules is presented.

Index Terms—Soft robot applications; modeling, control, and learning for soft robots; biologically-inspired robots; marine robotics.

Costanza Armanini and Madiha Farman are with the Department of Mechanical Engineering, Khalifa University of Science, and Technology, Abu Dhabi, UAE (e-mail: costanza.armanini@ku.ac.ae; madiha.farman@ku.ac.ae).

Marcello Calisti is with the Lincoln Institute for Agri-Food Technology, University of Lincoln, Lincoln LN6 7TS, U.K. (e-mail: MCalisti@lincoln.ac.uk).

Francesco Giorgio-Serchi is with the Institute of Integrated Micro and Nano Systems, University of Edinburgh, Edinburgh EH8 9YL, U.K. (e-mail: f.giorgio-serchi@ed.ac.uk).

Cesare Stefanini is with the The BioRobotics Institute, Scuola Superiore Sant'Anna, Pisa 56127, Italy, also with the Khalifa University Center for Autonomous Robotic Systems (KUCARS), Khalifa University of Science and Technology, Abu Dhabi, UAE, and also with the Healthcare Engineering Innovation Center (HEIC), Khalifa University of Science and Technology, Abu Dhabi, UAE (e-mail: c.stefanini@sssup.it).

Federico Renda is with the Department of Mechanical Engineering, Khalifa University of Science, and Technology, Abu Dhabi, UAE, and also with the Khalifa University Center for Autonomous Robotic Systems (KUCARS), Khalifa University of Science and Technology, Abu Dhabi, UAE (e-mail: federico.renda@ku.ac.ae).

This article has supplementary material provided by the authors and color versions of one or more figures available at https://doi.org/10.1109/TRO.2021.3094051.

Digital Object Identifier 10.1109/TRO.2021.3094051

I. INTRODUCTION

ROBOTICS is pushing forward the boundary of exploration, aiming toward remote planets in space and deep waters within our oceans. Either for commercial or scientific purposes, humans depend on robotic intervention to operate in such extreme environments, where pressure, temperature, and lack of illumination prevent scuba diving and human presence. The role of robotics is predominant with respect to human intervention also in shallow water: longer operation times, resilience to atmospheric conditions, and reduced human risk are just a few among the many advantages that motivate the employment of robots over humans. However, remotely operated and unmanned underwater vehicles have been introduced to replace human divers in underwater operations with incomplete success. While they have been successfully applied to safely patrol open stretches of sea, they still present severe limitations in manipulation, close structure monitoring, and locomotion within cluttered environments. In particular, they suffer from nonnegligible limitations when navigating close to the seabed or near submerged structures, where unintended impacts must be prevented consistently.

For all these reasons, some researchers suggested a radically different approach toward the soft robotics paradigm. Soft robotics appears, both in land and especially in water, as a promising alternative to allow safer, simpler, and cost-effective interactions with the environment. The increasing interest in the use of compliant and soft material stirred the development of several underwater soft robots, which exploited the compliance in their body to increase their own performance, or to grant new capabilities to underwater vehicles.

Within the context of aquatic organisms, major sources of inspiration have been drawn from fish and cephalopods [1]–[7]. Looking at swimming microorganisms, a crucial source of inspiration for soft propellers comes from prokaryotic flagellum [8] [9], which is considered as the only known example of a biological "wheel" [10]. Its simple rotary propulsion mechanism makes it similar to traditional propellers and more practical with respect to other existing soft underwater robots based on oscillatory motion. A great number of flagellum-inspired prototypes exists, characterized by a stiff structure and ranging in size in the micrometre scale [11], operating in the low-Reynolds number regime. In [12], artificial swimmers with flexible tail shown nontrivial dependence of swimming speed and direction on actuation frequency under a rotating magnetic field, but these were also ranging at the micrometer scale. A macroscopic

experimental investigation of the elastic trail propulsion mechanism is presented in [13], where a high viscosity fluid is considered to restrict the analysis at the low-Reynold number regime. A soft macroscale propeller inspired by prokaryotik flagella has been recently proposed in [14]. In this previous work by the authors, the design of the prototype has been presented and a first set of trials has been conducted in a controlled environment to assess the propulsive thrust. Here, we extend and improve the results to propose a first class of macroscale soft underwater vehicles inspired by flagellated bacteria. In particular, we provide a theoretical model to investigate the propulsive capabilities of the macroscale flagellar modules, which are hybrid rigid-soft elements made up of three components. In this article, the final structure resembles the one of the prokaryotic flagellum, but a great number of solutions can be generated by the combination of different designs of the three components, paving the way to a new family of soft underwater robots. Finally, we present an underwater vehicle, which is propelled by combination of four flagellar modules. This article is organized as follows. Section II presents the bioinspired design of the flagellar propulsive modules and their fabrication. In Section III, the theoretical model is presented, with particular attention to the description of the action of the fluid on the modules, which generates the propulsive thrust. Section IV presents the theoretical and experimental analysis that have been carried out to complete and validate the theoretical model. Section V provides two experimental set-ups that are employed to perform a first estimation of the propulsive capabilities of the single flagellar module. Section VI presents the design, fabrication, and experimental tests of an underwater vehicle prototype, which, similarly to aerial quadrotors, combines the action of four propellers to move in different directions. Finally, Section VII draws the conclusive discussion on the obtained results and on the future developments of the proposed research.

II. BIO-INSPIRED DESIGN AND FABRICATION

By taking inspiration from the prokaryotic monotrichous bacteria [15], we designed a novel kind of soft propeller embedding the principal components of the bacteria's flagellum (see Fig. 1) and ranging in the macroscale size. The natural flagellum is made of two main components: the *hook*, which is the short proximal part of the flagellum, and the *filament*, which is the long distal part. An actuation structure, the *flagellar motor*, connects the flagellum with the cell's body and rotates the hook, which eventually transmits the torque to the filament.

The interaction between the elastic component of the flagellum and the surrounding fluid creates the onset of helical waves [17], which finally propel the bacteria forward, or backward, depending on the travel direction of the wave [15]. Soft mobile robots, thanks to their deformable bodies or appendages, could exploit simple actuation strategies to achieve complex and rich behaviors [2]. With this respect, the prokaryotik flagella represents a perfect biological model to exploit the different mechanical properties of the *hook* [18] and the *filament* [19] under the effect of a simple rotational actuation granted by the *flagellar motor* [20]. Moreover, the hook shows high resistance
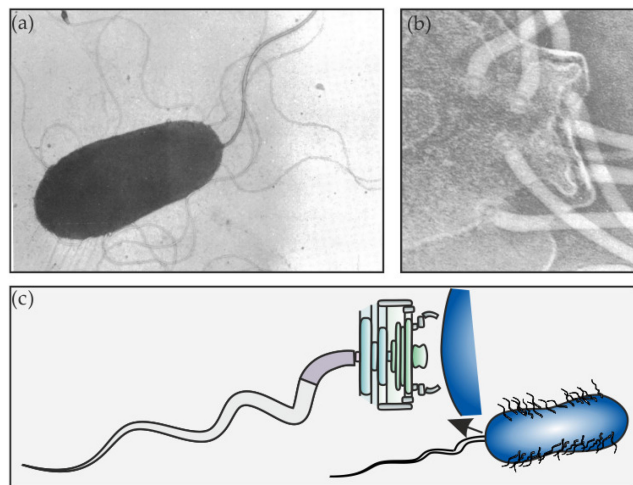

Fig. 1. (a) *B. parahaemolytica* and (b) the basal discs of the flagella of *P. fischeri*, [16]. (c) Schematics of the flagellum structure with the *flagellar motor*.
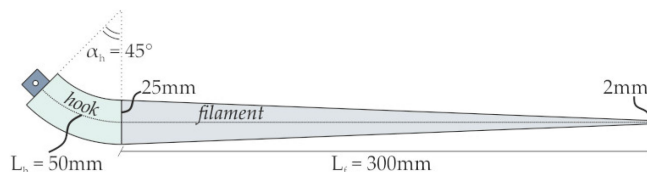

Fig. 2. Sketch of the flagellum design.

to torsional strain, ensuring the transmission of the torque from the flagellar motor to the filament. These two features allow a high number of possible kinematics, which would not be possible with a flagellum made of an homogeneous structural material [21]. Since the final shape of the flagellum, and thus the locomotion performances of the bacteria, emerges as an interplay between the fluid, the flagellum mechanical properties, and the actuation frequency of the motor, it could be preferable to investigate the structural response of such passive elements without *a priori* imposing a certain helical shape (i.e., a rigid appendage) [11], [15].

A. Flagellar Module Design and Fabrication

The propeller's final design has been first presented in [14]. Following the abovementioned specifications, the soft module is composed of a cylindrical *hook*, having a length $L_h = 50$ mm and a precurvature $\alpha_h = 45°$, and a conical *filament* 300 mm long, with a diameter varying from 2 to 25 mm (see Fig. 2).

The flagellum is made out of silicone, while the torsional stiffness of the hook has been achieved with an ABS backbone, specifically designed and cast inside the silicone. After being vacuum degassed, the silicone is injected in a Teflon mold that has been fabricated via CNC machining. Using a Teflon made mold, there is no need to use any release agent, significantly easing the casting process. The 3D-printed backbone of the *hook*, including the attachment to the motor's shaft, is inserted in the mold before proceeding with the injection (see Fig. 3).

Different parameters and variables affect the net propulsive thrust of the proposed device. These include the density of the
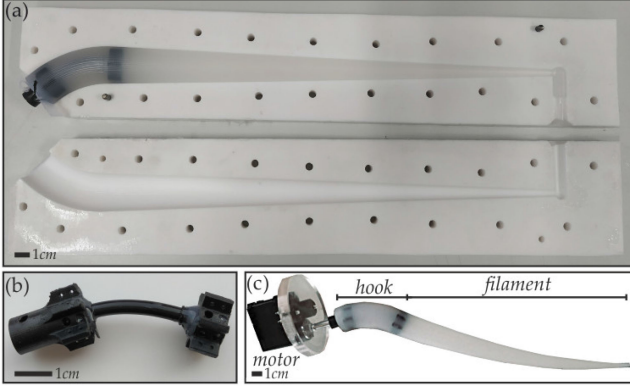
Fig. 3. (a) A Teflon mold has been used to fabricate the flagellar modules. (b) The ABS backbone used to achieve the torsional stiffness of the *hook*. (c) Final design of the flagellum, with the motor attached to the *hook* through a stainless steel shaft.
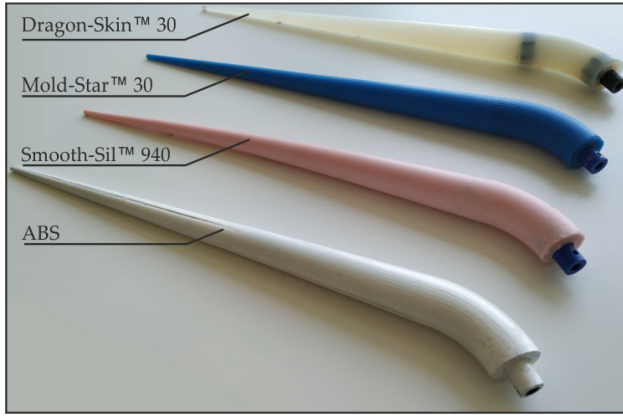

Fig. 4. Flagellar modules that have been fabricated and tested. Three different silicones have been used, varying in their stiffness, while a rigid ABS propeller has been 3D-printed. The material's properties are reported in Table I.

TABLE I
MATERIALS PROPERTIES

Material	100% Modulus E [Pa]	Density ρ [kg/m^3]
Dragon Skin™ 30	$592.95 \cdot 10^3$	1080
Mold Star™ 30	$661.90 \cdot 10^3$	1121
Smooth Sil™ 940	$1378.95 \cdot 10^3$	1183
ABS	$1681 \cdot 10^6$	1050

material employed for fabricating the flagellum, the frequency of the motion and the viscosity of the fluid. Here, we focus mostly on the different performances that can be obtained at varying the deformed shapes of the propeller, namely the helical waves, which are obtained at varying the material stiffness and the rotational speed of the motor. For this reason, three different silicones have been used to fabricate the flagellar modules, all from Smooth-Sil™. Finally, a rigid flagellum, made out of ABS, has been 3D-printed to compare the behavior that can be attained using a material that does not allow the onset of the helical waves along the filament. Fig. 4 presents the four flagellar modules, while the main properties of the employed materials are reported in Table I.
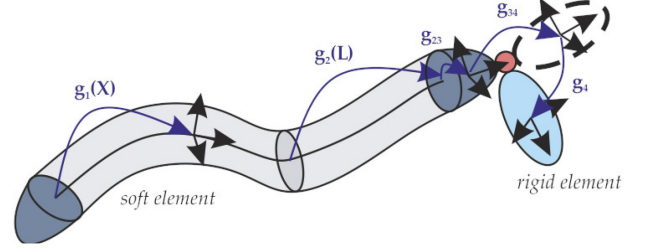

Fig. 5. Schematics of the kinematics of a soft-rigid multi-body system: $\boldsymbol{g}_{ij}\boldsymbol{g}_j$ represents the jth body position and orientation with respect to the ith body and $X_i \in [0 \; L_i]$ is the soft body curvilinear abscissa ($X_i = 1$ for rigid bodies).

An ad-hoc designed stainless steel shaft is used to connect the *hook*'s backbone to an MX28-AT *Dynamixel* servomotor by ROBOTIS. In particular, with respect to other similar servomotors, the MX28-AT allows the control of the propeller in wheel mode, maintaining a predefined constant rotatory speed. The motor is contained in a waterproof container and is controlled by an Arbotix-M Robocontroller, an Arduino compatible microcontroller specifically made for *Dynamixel* actuators. Both the board and the motor are power by a 11.1 V, 2200 mAh Li-Po battery. Two XBee 1 mW Wire antennas are used to initiate the rotation of the motor and to continuously track the actuation speed.

III. DYNAMICAL MODELING

The elastodynamics of the proposed hybrid soft-rigid design is described through the geometric and unifying approach developed in [22] and [23], which is a generalization to soft and hybrid systems of the geometric theory of rigid robots due to Brockett [24]. For further details, the interested reader is referred to [22]. According to this formulation, the configuration of the ith soft/rigid body with respect to the spatial frame is defined as a curve $\boldsymbol{g}_i(\cdot) : X_i \to \boldsymbol{g}_i(X_i) \in SE(3)$, given by the following:

$$\boldsymbol{g}_i(X_i) = \begin{pmatrix} \boldsymbol{R}_i(X_i) & \boldsymbol{u}_i(X_i) \\ 0^T & 1 \end{pmatrix} \in SE(3) \qquad (1)$$

where $X_i \in [0 \; , L_i]$ is the soft body curvilinear abscissa ($X_i = 1$ for rigid bodies), $\boldsymbol{R}_i(X_i) \in SO(3)$ is the orientation matrix and $\boldsymbol{u}_i(X_i) \in \mathbb{R}^3$ is the position vector. The configuration space is parametrized by the traditional generalized variables for the rigid components and by a subspace of the 6-D local strain space for the soft ones, defined in (2). A schematics of the kinematics of soft-rigid hybrid systems is reported in Fig. 5. The continuous models of the position, velocity, and acceleration of a soft body can be derived from the Cosserat rod theory, which gives [25]

$$\begin{aligned} \boldsymbol{g}_i'(X_i) &= \boldsymbol{g}_i(X_i)\widehat{\boldsymbol{\xi}}_i(X_i) \\ \dot{\boldsymbol{g}}_i(X_i) &= \boldsymbol{g}_i(X_i)\widehat{\boldsymbol{\eta}}_i(X_i) \\ \boldsymbol{\eta}_i'(X_i) &= \dot{\boldsymbol{\xi}}_i(X_i) - \mathrm{ad}_{\boldsymbol{\xi}_i(X_i)}\boldsymbol{\eta}_i(X_i) \\ \dot{\boldsymbol{\eta}}_i'(X_i) &= \ddot{\boldsymbol{\xi}}_i(X_i) - \mathrm{ad}_{\dot{\boldsymbol{\xi}}_i(X_i)}(X_i)\boldsymbol{\eta}_i(X_i) - \mathrm{ad}_{\boldsymbol{\xi}_i(X_i)}\dot{\boldsymbol{\eta}}_i(X_i) \end{aligned} \qquad (2)$$

where
1) $\boldsymbol{\xi}_i(X_i)$ defines the strain state:

$$\widehat{\boldsymbol{\xi}}_i(X_i) = \begin{pmatrix} \tilde{\mathsf{k}}_i & \mathsf{p}_i \\ \mathbf{0}^T & 0 \end{pmatrix} \in \mathfrak{se}(3) \ , \ \boldsymbol{\xi}_i(X_i) = \left(\mathsf{k}_i^T, \mathsf{p}_i^T\right)^T \in \mathbb{R}^6$$

where $\tilde{\mathsf{k}}_i(X_i) \in \mathfrak{so}(3)$, $\mathsf{k}_i(X_i) \in \mathbb{R}^3$ and $\mathsf{p}_i(X_i) \in \mathbb{R}^3$ are, respectively, the angular and linear strain

2) $\boldsymbol{\eta}_i(X_i)$ is the cross-section velocity twist

$$\widehat{\boldsymbol{\eta}}_i(X_i) = \begin{pmatrix} \tilde{\mathsf{w}}_i & \mathsf{v}_i \\ \mathbf{0}^T & 0 \end{pmatrix} \in \mathfrak{se}(3) \ , \ \boldsymbol{\eta}_i(X) = \left(\mathsf{w}_i^T, \mathsf{v}_i^T\right)^T \in \mathbb{R}^6$$

where $\tilde{\mathsf{w}}_i(X_i) \in \mathfrak{so}(3)$, $\mathsf{w}_i(X_i) \in \mathbb{R}^3$, and $\mathsf{v}_i(X_i) \in \mathbb{R}^3$ are, respectively, the angular and linear velocity

$(\cdot)' = \frac{\partial(\cdot)}{\partial X_i}$, $\dot{(\cdot)} = \frac{\partial(\cdot)}{\partial t}$ and $\mathrm{ad}_{(\cdot)} \in \mathbb{R}^{6 \times 6}$ is the adjoint operator of the Lie algebra (see Appendix A). In the above expressions, the tilde represents the isomorphism between 3-D vectors and skew symmetric matrices (see Appendix A). To model a constrained rod, a constant strain is assumed along the section jth, providing

$$\boldsymbol{\xi}_j - \boldsymbol{\xi}_j^* = \boldsymbol{B}_j \boldsymbol{q}_j \tag{3}$$

where $j > i$ are body (or section) indexes and $\boldsymbol{B}_j \in \mathbb{R}^{6 \times n_j}$ is the basis for the subspace of motion allowed by the jth joint (or strain) and the body generalized coordinate $\boldsymbol{q}_j \in \mathbb{R}^{n_j}$ (n_j being the number of degrees of freedom of the jth body). $\boldsymbol{\xi}_j^* \in \mathbb{R}^6$ is the elastic joint (or strain) reference value, which is equal to zero for lumped inelastic joints. Assuming piece-wise constant strains [26], equations (2) can be analytically integrated in space using the matrix exponential method, leading to the kinematics of a hybrid system

$$\begin{cases} \boldsymbol{g}_j(X_j) = e^{X\widehat{\boldsymbol{\xi}}_j} \\ \boldsymbol{\eta}_j(X_j) = \mathrm{Ad}_{\boldsymbol{g}_{ij}\boldsymbol{g}_j(X_j)}^{-1} \boldsymbol{\eta}_i + \mathrm{Ad}_{\boldsymbol{g}_j(X_j)}^{-1} \mathrm{T}_{\boldsymbol{\xi}_j}(X_j) \boldsymbol{B}_j \dot{\boldsymbol{q}}_j \end{cases} \tag{4}$$

where X_j is taken along the jth discrete section. Following the assumption of constant strains, equation (4)$_1$ provides the jth body position and orientation $\boldsymbol{g}_j \in SE(3)$ thorough the exponential mapping of the joint or strain twist. Finally, equation (4)$_2$ provides the jth body velocity twist $\boldsymbol{\eta}_j \in \mathbb{R}^6$, where $\boldsymbol{g}_{ij}\boldsymbol{g}_j \in SE(3)$ is the jth body position and orientation with respect to the ith body, while $\mathrm{Ad}_{\boldsymbol{g}_j}$ and $\mathrm{T}_{\boldsymbol{\xi}_j} \in \mathbb{R}^{6 \times 6}$ are, respectively, the adjoint and tangent operator of the exponential map (see Appendix A). Successive applications of equations (4) to all the bodies of the hybrid system, yields to the definition of the geometric Jacobian $\boldsymbol{J}_j \in \mathbb{R}^{6 \times n}$ for each soft/rigid body (n being the total number of DoFs), which relates the generalized coordinate vector $\boldsymbol{q} \in \mathbb{R}^n$ and the jth body velocity twist $\boldsymbol{\eta}_j$ [22]

$$\boldsymbol{\eta}_j(X_j) = \sum_{i=0}^{j} \mathrm{Ad}_{\boldsymbol{g}_i \cdots \boldsymbol{g}_j}^{-1} \int_0^{L_i \text{ or } X_j} \mathrm{Ad}_{\boldsymbol{g}_i} \, ds \boldsymbol{B}_i \dot{\boldsymbol{q}}_i =$$
$$= \sum_{i=0}^{j} {}^j\boldsymbol{S}_i \dot{\boldsymbol{q}}_i = \boldsymbol{J}_j(X_j)\dot{\boldsymbol{q}} . \tag{5}$$

Equation (5) defines the geometric Jacobian of jth body $\boldsymbol{J}_j(X_j) = [{}^j\boldsymbol{S}_0 \, {}^j\boldsymbol{S}_1 \cdots {}^j\boldsymbol{S}_N] \in \mathbb{R}^{6 \times n}$, where N is the total number of bodies. The free dynamic equation is obtained, for a rigid body is

$$\boldsymbol{\mathcal{M}}_i \dot{\boldsymbol{\eta}}_i + \mathrm{ad}_{\boldsymbol{\eta}_i}^* \boldsymbol{\mathcal{M}}_i \boldsymbol{\eta}_i = \boldsymbol{\mathcal{F}}_{J_i} - Ad_{\boldsymbol{g}_{ij}\boldsymbol{g}_j}^* \boldsymbol{\mathcal{F}}_{J_j} + \boldsymbol{\mathcal{F}}_{e_i} \tag{6}$$

where $\boldsymbol{\mathcal{M}}_i \in \mathbb{R}^{6 \times 6}$ represents the screw inertia matrix of the rigid body, $\boldsymbol{\mathcal{F}}_{J_i}$ and $\boldsymbol{\mathcal{F}}_{J_j} \in \mathbb{R}^6$ are the internal load transferred through joints i and j, respectively, while $\boldsymbol{\mathcal{F}}_{e_i} \in \mathbb{R}^6$ is the concentrated external load.

For a soft body, the free dynamics equations with their boundary conditions are

$$\bar{\boldsymbol{\mathcal{M}}}_i \dot{\boldsymbol{\eta}}_i + \mathrm{ad}_{\boldsymbol{\eta}_i}^* \bar{\boldsymbol{\mathcal{M}}}_i \boldsymbol{\eta}_i = \boldsymbol{\mathcal{F}}_{i_i}' + \mathrm{ad}_{\boldsymbol{\xi}_i}^* \boldsymbol{\mathcal{F}}_{i_i} + \bar{\boldsymbol{\mathcal{F}}}_{e_i}$$
$$\boldsymbol{\mathcal{F}}_{i_i}(0) = -\boldsymbol{\mathcal{F}}_{J_i} \quad , \quad \boldsymbol{\mathcal{F}}_{i_i}(L_i) = -Ad_{\boldsymbol{g}_{ij}}^* \boldsymbol{\mathcal{F}}_{J_i} . \tag{7}$$

Above, $\bar{\boldsymbol{\mathcal{M}}}_i \in \mathbb{R}^{6 \times 6}$ is the screw inertia density matrix of the cross section, $\bar{\boldsymbol{\mathcal{F}}}_{e_i} \in \mathbb{R}^6$ is the distributed external load, $\bar{\boldsymbol{\mathcal{F}}}_{i_i} \in \mathbb{R}^6$ is the internal wrench due to the elasticity of the soft body. A linear elastic model is employed, since this assumption very well describes the behavior of the considered rubber-like materials up to 100% elongations:

$$\bar{\boldsymbol{\mathcal{F}}}_{i_i} = \boldsymbol{\Sigma}_i \boldsymbol{B}_i \boldsymbol{q}_i \tag{8}$$

where $\boldsymbol{\Sigma}_i = \mathrm{diag}(G J_{x_i}, E_i J_{y_i}, E_i J_{z_i}, E_i A_i, G_i A_i, G_i A_i)$, E is Young's modulus, G is the shear modulus, A is the section area, and J_y, J_z, and J_x are, respectively, the bending and torsion second moment of area of the beam cross section. Once a Jacobian is found from (5), the generalized dynamics of the hybrid system can be obtained by projecting the free dynamics of each body, both rigid (6) and soft (7), by virtue of the D'Alembert's principle. For further details, the reader is referenced to Appendix B and to the previous works by the authors [22] and [23]. Thus, we obtain the generalized dynamic equations of the hybrid system in the standard form

$$\boldsymbol{M}(\boldsymbol{q})\ddot{\boldsymbol{q}} + \boldsymbol{C}(\boldsymbol{q}, \dot{\boldsymbol{q}})\dot{\boldsymbol{q}} + \boldsymbol{K}\,\boldsymbol{q} = \boldsymbol{\tau} + \boldsymbol{F}(\boldsymbol{q}, \dot{\boldsymbol{q}}) \tag{9}$$

1) $\boldsymbol{M} \in \mathbb{R}^{n \times n}$ is the mass matrix

$$\boldsymbol{M}(\boldsymbol{q}) = \sum_{i=0}^{N} \int_0^{L_i} \boldsymbol{J}_i^T \bar{\boldsymbol{\mathcal{M}}} \boldsymbol{J}_i dX_i \tag{10}$$

2) $\boldsymbol{C} \in \mathbb{R}^{n \times n}$ is the Coriolis matrix

$$\boldsymbol{C}(\boldsymbol{q}, \dot{\boldsymbol{q}}) = \sum_{i=0}^{N} \int_0^{L_i} \boldsymbol{J}_i^T \left(ad_{\boldsymbol{\eta}_i}^* \bar{\boldsymbol{\mathcal{M}}} \boldsymbol{J}_i + \bar{\boldsymbol{\mathcal{M}}} \dot{\boldsymbol{J}}_i\right) dX_i \tag{11}$$

where
3) $\boldsymbol{K} \in \mathbb{R}^{n \times n}$ is the stiffness matrix

$$\boldsymbol{K} = \mathrm{diag}_{i=0}^{N} \left(\boldsymbol{B}_i^T \int_0^{L_i} \boldsymbol{\Sigma}_i dX_i \boldsymbol{B}_i\right) \tag{12}$$

4) $\boldsymbol{\tau} \in \mathbb{R}^n$ is the actuation vector
5) $\boldsymbol{F} \in \mathbb{R}^n$ is the generalized external force vector, which includes the action of the gravity and the fluid on the body.

$$\boldsymbol{F}(\boldsymbol{q}, \dot{\boldsymbol{q}}) = \sum_{i=0}^{N} \int_0^{L_i} \boldsymbol{J}_i^T \bar{\boldsymbol{\mathcal{F}}}_{e_i} dX_i \tag{13}$$

The above expressions are valid for a soft element, while the rigid case can be easily recovered removing the integrals and replacing the distributed quantities with their lumped counterparts. Moreover, in general, for a rigid link $\boldsymbol{\tau}_i = {}^i\boldsymbol{S}_i^T \boldsymbol{\mathcal{F}}_{J_i}$.

A. Hydrodynamical Modeling

The dynamic interaction between the soft *filament* and the surrounding fluid represents the foundation of the propulsive mechanism of the flagellar modules. The *filament* deforms as a consequence of the action of the fluid, which, at the same time, is affected by the movement and rotation of the module. The complete description of such an highly coupled fluid-structure interaction requires a deep investigation, possibly with the support of CFD software, which goes beyond the scope of the proposed paper and that will be subject of further investigation in future works. Here, we propose a simplified model that allows the decoupling of the two problems. In particular, in the proposed model, the action of the fluid on the ith body is included in the external force vector as

$$\boldsymbol{\mathcal{F}}_e = \boldsymbol{\mathcal{F}}_{e,G} + \boldsymbol{\mathcal{F}}_{e,B} + \boldsymbol{\mathcal{F}}_{e,A} + \boldsymbol{\mathcal{F}}_{e,D} \quad \text{for rigid bodies}$$
$$\bar{\boldsymbol{\mathcal{F}}}_e = \bar{\boldsymbol{\mathcal{F}}}_{e,G} + \bar{\boldsymbol{\mathcal{F}}}_{e,B} + \bar{\boldsymbol{\mathcal{F}}}_{e,A} + \bar{\boldsymbol{\mathcal{F}}}_{e,D} \quad \text{for soft bodies} \tag{14}$$

where we omitted the ith subscript for sake of clarity. The subscripts G, B, A refer to the gravity, buoyancy, and added mass components of the external force, respectively, while the subscript D represents the drag and lift components. In the following, all the local reference systems are positioned in the geometric centers of the bodies, with the x axis for the flagellar module corresponding to the axis tangent to the midline, while for the rigid canister the y axis corresponds to its axis of symmetry.

1) Gravity and Buoyant Force: The external force vector includes the action the buoyant force and the weight of the body, both acting in the vertical direction in the world reference system. Following Archimedes' principle and assuming a uniform density of the fluid ρ_w, the buoyant force is directly proportional to the volume of the displaced fluid and the fluid's density. This force is applied to the geometric center of the displaced volume of fluid, which coincides with the entire external volume of the body V_{ext}. For the soft, continues bodies with uniform mass distribution, the combination of the weight and the buoyant force is given by

$$\bar{\boldsymbol{\mathcal{F}}}_{e,G} + \bar{\boldsymbol{\mathcal{F}}}_{e,B} = \left(1 - \frac{\rho_w}{\rho}\right)\bar{\boldsymbol{\mathcal{M}}}\boldsymbol{\mathcal{G}} \tag{15}$$

where ρ is the body's density and $\boldsymbol{\mathcal{G}}$ is the gravity vector in the local reference system (whose rotational components are null). When the weight is not uniformly distributed, for example, for the canister containing the motor and other electronic components, the weight and the buoyant force should be calculated separately. In particular, the weight is obtained through the definition of the body total inertia matrix, given by the sum of the inertia matrices of all the components, projected in the body's reference system, namely

$$\boldsymbol{\mathcal{M}} = \sum_k Ad_{g_k}^* \boldsymbol{\mathcal{M}}_k Ad_{g_k^{-1}} \tag{16}$$

where k spans among the weights composing the body, $\boldsymbol{\mathcal{M}}_k$ is the inertia matrix of the kth components in its local reference system and Ad_g^* is the coAdjoint representation of SE(3) (see Appendix A). Following this procedure, the total inertia mass matrix $\boldsymbol{\mathcal{M}}$ resembles the following structure [27]:

$$\boldsymbol{\mathcal{M}} = \begin{pmatrix} \boldsymbol{\mathcal{I}} & m\widetilde{\boldsymbol{c}} \\ m\widetilde{\boldsymbol{c}}^T & mI_3 \end{pmatrix} \in \mathbb{R}^{6\times 6} \tag{17}$$

where $\boldsymbol{\mathcal{I}} \in \mathbb{R}^{3\times 3}$ represents the rotational inertia of the body, m is its total mass, $\boldsymbol{c} \in \mathbb{R}^3$ is the position of the center of gravity with respect to the body's reference system and I_3 is 3×3 identity matrix. Once the total inertia matrix is found, the resultant of the weight and the buoyancy force is

$$\boldsymbol{\mathcal{F}}_{e,G} + \boldsymbol{\mathcal{F}}_{e,B} = \boldsymbol{\mathcal{M}}\boldsymbol{\mathcal{G}} - \rho_w V_{ext}\boldsymbol{\mathcal{G}} . \tag{18}$$

2) Added Mass: The added mass matrix $\boldsymbol{\mathcal{M}}_A$ models the volume of fluid accelerated around the body. It represents the reactive, inertial forces caused by the interaction with the fluid, which are not negligible in the high *Reynolds* number domain and when slender bodies are considered [28]. The action of the added mass is obtained as follows:

$$\boldsymbol{\mathcal{F}}_{e,A} = -\boldsymbol{\mathcal{M}}_A\dot{\boldsymbol{\eta}} , \qquad \bar{\boldsymbol{\mathcal{F}}}_{e,A} = -\bar{\boldsymbol{\mathcal{M}}}_A\dot{\boldsymbol{\eta}}. \tag{19}$$

The added mass matrices for the different modeled elements are defined as follows:

$$\bar{\boldsymbol{\mathcal{M}}}_A = \pi R(X)^2 \, \rho_w \, diag\,[0, 0, 0, 0, B_y, B_z]$$
$$\boldsymbol{\mathcal{M}}_A = \rho_w \, V_{ext} diag\left[\gamma, 0, \gamma, \frac{\beta}{2-\beta}, \frac{\lambda}{2-\lambda}, \frac{\beta}{2-\beta}\right] . \tag{20}$$

It should be noted that the off-diagonal terms of the added mass matrix might be non-null but, as previously mentioned, through a parallelism with rigid blades, these terms are neglected for sake of simplicity. In $(20)_1$, $R(X) \in \mathbb{R}$ is the radius of the flagellum in X, while $B_y = B_z = 0.6$ are the added mass coefficients in the y and z direction. For sake of simplicity, the rigid body is approximated to a symmetric prolate ellipsoid with radius R_b and total length L_b. Following this approximation, the added mass terms λ, β, and γ in $(20)_2$ are [29]:

$$\lambda = \frac{2(1-\epsilon^2)}{\epsilon^3}\left(\frac{1}{2}\log\left(\frac{1+\epsilon}{1-\epsilon}\right) - \epsilon\right)$$
$$\beta = \frac{1}{\epsilon^2} - \frac{(1-\epsilon^2)}{2\epsilon^3}\log\left(\frac{1+\epsilon}{1-\epsilon}\right)$$
$$\gamma = \frac{\lambda - \beta}{5}\left[\frac{\left(R_b^2 - \frac{L_b^2}{4}\right)^2}{2\left(R_b^2 - \frac{L_b^2}{4}\right) + (\beta - \lambda)\left(R_b^2 + \frac{L_b^2}{4}\right)}\right] \tag{21}$$

where $\epsilon = 1 - 4(\frac{R_b}{L_b})^2$ is the eccentricity of the body.

3) Drag and Lift Forces: Regarding the modeling of the fluid-structure interaction in the external force vector, we employ the simplified Lighthill 3-D large amplitude elongated body theory [30], where the fluid action is represented by a distributed

force along the flagellum, given by

$$\bar{\mathcal{F}}_{e,D}(X) = -\bar{\mathcal{D}}(X)\|\mathsf{v}(X)\|\boldsymbol{\eta}(X)$$
$$\mathcal{F}_{e,D} = -\boldsymbol{\mathcal{D}}\|\mathsf{v}\|\boldsymbol{\eta}. \tag{22}$$

In (22), $\mathsf{v}(X) \in \mathbb{R}^3$ is the translational part of the velocity twist $\boldsymbol{\eta}(X)$, while $\boldsymbol{\mathcal{D}}(X) \in \mathbb{R}^{6\times6}$ is the screw matrix of the drag and lift coefficients. Through this formulation, the action of the fluid is decomposed in a resistive (drag) and a conservative (lift) part. While the drag force varies mostly with the *Reynolds* number *Re* of the structure and acts opposite to the flow direction, the lift force is mostly due to the circulation of the flow around the body induced by the radial gradient of the velocity (Kutta–Joukowski theorem) and it acts perpendicular to it. Following the classical aerodynamics theory of propulsive systems, shear stresses and edge effects are neglected for sake of simplicity. This assumption would not be valid at low Reynolds numbers, while, in our case, the order of magnitude of the Reynolds number *Re* has been estimated to be $\simeq 10^4$. Finally, the drag and lift matrix $\boldsymbol{D}$ is modeled as follows:

$$\bar{\boldsymbol{D}}(X) = R(X)\rho_w \begin{bmatrix} 0 & \cdots & & & & 0 \\ 0 & \cdots & & & & 0 \\ 0 & \cdots & & & & 0 \\ 0 & \cdots & 0 & 0 & 0 \\ 0 & \cdots & 0 & C_D & -C_L \\ 0 & \cdots & 0 & C_L & C_D \end{bmatrix} \in \mathbb{R}^{6\times6} \tag{23}$$

where C_L is the lift coefficient along the x direction (the direction tangent to the cross section of the flagellum), while C_D is the drag coefficient acting on the y and z directions. The procedure employed to obtain the drag and lift coefficients composing matrix (23) for the soft and the rigid flagella is detailed in the following Section IV. Moving to the rigid body, its drag and lift matrix component is obtained as follows:

$$\boldsymbol{D} = \frac{1}{2}\rho_w \, \mathrm{diag}\left[C_r A_x R_b^3, 0, C_r A_z R_b^3, C_x A_x, C_y A_y, C_z A_z\right] \tag{24}$$

where R_b is the body radius, A_x, A_y, and A_z are the cross-sectional areas of the body in the x, y, and z directions, respectively. The viscous coefficients have been estimated from the experimental results (see Sections V-A and VI), where $C_z = C_x$ for symmetry.

B. Motion Subspaces for the Flagellum Module and the Rigid Components

The proposed design is composed by one rigid body (the *flagellar motor*) and two soft components (the *hook* and the *filament*) having different elastic features. Each of these three components are therefore described by a specific model, which better represents their behavior. In particular, the *flagellar motor* is modeled as an actuated revolute joint, the *hook* is represented by an inextensible Cosserat rod with constant curvature and constrained torsion, while the *filament* is described by an inextensible Kirchhoff–Love rod. Accordingly, the motion subspaces are defined by the following basis and reference twists (assuming

the x-axis lying along the rotation axis for the revolute joint and along the midline tangent for the rods):

$$\boldsymbol{B}_m = \begin{bmatrix} 1 \\ 0 \\ 0 \\ 0 \\ 0 \\ 0 \end{bmatrix}, \boldsymbol{B}_h = \begin{bmatrix} 0 & 0 \\ 1 & 0 \\ 0 & 1 \\ 0 & 0 \\ 0 & 0 \\ 0 & 0 \end{bmatrix}, \boldsymbol{B}_f = \begin{bmatrix} 1 & 0 & 0 \\ 0 & 1 & 0 \\ 0 & 0 & 1 \\ 0 & 0 & 0 \\ 0 & 0 & 0 \\ 0 & 0 & 0 \end{bmatrix}, \boldsymbol{\xi}_h^* = \begin{bmatrix} 0 \\ \alpha_h/L_h \\ 0 \\ 1 \\ 0 \\ 0 \end{bmatrix}, \boldsymbol{\xi}_f^* = \begin{bmatrix} 0 \\ 0 \\ 0 \\ 1 \\ 0 \\ 0 \end{bmatrix} \tag{25}$$

where subscripts m, h, and f refer to the *motor*, the *hook*, and the *filament*, respectively. Regarding the canister, it is modeled according to the considered net motion of the body. In this article, two experimental trials are realized. In Section IV-B, a static setup is employed, with the motor and the canister held stationary, while in the second trials, Section V-A, the canister is constrained in a curvilinear motion through a marry-go-round set-up. Following these specifications, the net motion subspaces are defined by the following basis twists (assuming the x-axis is aligned with the heading):

$$\boldsymbol{B}_{b,1} = \boldsymbol{I}_{6x6}, \qquad \boldsymbol{B}_{b,2} = \begin{bmatrix} 0 \\ 1 \\ 0 \\ R_a \\ 0 \\ 0 \end{bmatrix}. \tag{26}$$

Above, $\boldsymbol{B}_{b,1}$ represent the basis used to model the first experimental set-up, where the controlled free motion is tested, while $\boldsymbol{B}_{b,2}$ is used to model the marry-go-round set-up of the second experiment, where R_a represents the radius of the curvilinear motion. In both cases, the rotation of the motor $\boldsymbol{q}_m(t) \in \mathbb{R}$ is prescribed, leading to two mixed forward-inverse dynamic problems. In the first experimental testing, the net displacement of the canister is prescribed and set to $\boldsymbol{q}_b = 0$, while the unknowns are the reaction forces/torques $\boldsymbol{\tau}_b(t) \in \mathbb{R}^6$. In the second experimental set-up, $\boldsymbol{\tau}_b$ is prescribed and set to 0, while $\boldsymbol{q}_b(t)$ is unknown, along with the torque exerted by the motor $\boldsymbol{\tau}_m(t)$ and the motion of the *hook* $\boldsymbol{q}_h(t)$ and the *filament* $\boldsymbol{q}_f(t)$. Both mixed problems can be solved by inverting and numerically integrating a proper recombination of the columns of (9) (see[31, example 9.1]). Equivalently, the recursive algorithm described in [23], can be employed.

It should be noted that the employed exponential coordinates parametrization has only local validity. For this reason, for the rigid body having $\boldsymbol{B}_{b,1}$, the exponential map should be regularly updated, i.e., at a generic updating time t the initial conditions should be reset as

$$\begin{Bmatrix} \boldsymbol{g}_0 \\ \boldsymbol{\xi}_b \\ \dot{\boldsymbol{\xi}}_b \end{Bmatrix} \Longleftarrow \begin{Bmatrix} \boldsymbol{g}_0 e^{\widehat{\boldsymbol{\xi}}_b(t)} \\ \boldsymbol{0}_{6\times1} \\ \boldsymbol{\eta}_b(t) \end{Bmatrix} \tag{27}$$

where $\boldsymbol{g}_0$ represents the last updated configuration, $\boldsymbol{0}_{6\times1}$ is a 6×1 zeros vector. In this way, the body coordinates $\boldsymbol{\xi}_b$ are set back to zero. The accuracy of the theoretical model in capturing

the elastodynamic of the system depends on the number of finite constant strain segments employed to discretize the *filament*. In [14], a constrained linear motion of the prototype has been simulated, computing the steady state forward speed of the body with respect to the angular speed of the motor. The test has been repeated increasing the number of segments used to discretize the *filament*, looking for convergence of the control parameter (i.e., swimming speed). Finally, it was found that, while the model generated nonphysical behavior for a 2-sections *filament* at high rotational speed, no significant differences were observed for a 3, 4, and 5, sections cases. Thus, the 3-sections model is selected for all the following simulations.

IV. DRAG AND LIFT COEFFICIENTS DEPICTION

In this section, we present the procedure employed for the definition of the drag and lift coefficients composing matrix (23). For the rigid propeller, the coefficients can be estimated using the formulations available in literature for the modeling of the aerodynamics of rigid airfoils. The procedure is summarized in Section IV-A, where the final coefficients are obtained. For the soft propellers, these formulations are not suitable anymore, in particular because the angle of attack of the fluid (namely the angle between the water flow and the section of the propeller) is not constant along the length of the propeller, which is highly deformed. The coefficients are functions of the geometry of the propeller and of the properties of the fluid. The exact determination of the coefficients based on these quantities is however particularly complicated because of the high deformations involved in the problem. For this reason and for sake of simplicity, we decided to estimate the values of the coefficients employing the results of the experiment described in Section IV-B.

A. Rigid Flagellum

Using one of empirical formulations that can be found in literature, the drag and lift coefficients can be *a priori* estimated for a rigid flagellum, where the direction between the section and the flow is fixed by the geometry of the module itself. For example, the drag coefficient can be estimated using the formula by Munson [32], valid for $Re < 10^7$

$$C_D = 1.17 + \frac{5.93}{Re^{1/2}} \tag{28}$$

which is valid for a infinitely long cylinder and it provides an average drag coefficient $C_D \simeq 1.2$. In the considered case, the flagellum is a cone having a finite ratio between its length and its radius and thus, due to the presence of border effects, a smaller value $C_D = 1.1$ is presumed. Moving to the lift force, following the theory mostly used to model the aerodynamics of airfoils, it can be estimated imposing the Kutta–Joukowski theorem, under the assumption of perfect fluid

$$\mathcal{F}_{e,L} = \rho_w \, U \, \Gamma \, A \tag{29}$$

where U is the undisturbed speed of the fluid, $\Gamma = \oint \mathbf{u} \times d\mathbf{s}$ is the circulation of the fluid around the profile and A is the lateral cross section of the body. Considering the geometry of
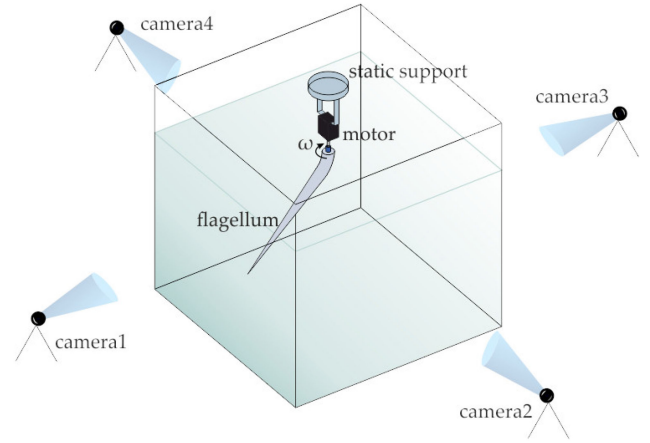

Fig. 6. Sketch of the static test set-up, where four cameras are placed along the sides of the tank to record the deformed shapes during the rotation of the flagella.

the flagellum, the lift coefficient is obtained

$$C_L = -2\pi \frac{R(X)}{R_\alpha} \frac{\cos \alpha_h}{\cos \delta_f} \tag{30}$$

where R_α is the radius of rotation, δ_f is the angle of the cone, and the negative sign is due to the negative circulation when a positive angular speed is considered. Finally, (30) provides an average lift coefficient $C_L \simeq -0.23$. Similarly to the drag coefficient, considering that the Kutta–Joukowski theorem (29) is valid for a cylinder in a stationary motion and under the assumption of perfect fluid, a smaller value $C_L = -0.1$ is presumed and employed in the simulations.

B. Soft Flagella

The empirical formulation presented for the rigid flagellum is not suitable for the depiction of the drag and lift coefficients for a soft propeller. As the motor rotates, the soft flagella interacts with the surrounding fluid and deforms resembling an helical shape that depends of many parameters, including the stiffness of the material and the rotational speed of the motor. For this reason and for sake of simplicity, the drag and lift coefficients composing matrix (23) for the soft propellers are here obtained performing a static experiment in a controlled environment, with the motor held stationary. In particular, the kinematics of the elastic *filament* are captured as a response to both the motor rotation and the interaction with the surrounding fluid. It should be noted that this is a simplification of the highly coupled fluid-structure interaction problem. In particular, we are gathering all the involved quantities in the definition of two coefficients C_L and C_D that are obtained from an evaluation of the deformed shapes obtained during the experiments.

Each flagellum is immersed in a 500×500 mm^2 tank of water and it is held vertically, with the motor attached to a fixed support unit. For each experiment, the motor rotates for 1 min at a fixed speed, both in clock-wise and counter-clockwise direction. Outside the tank, along its sides, four cameras are placed to record the whole experiment (see Figs. 6 and 7). Six markers have been drawn along the soft modules, two within the *hook*, and four
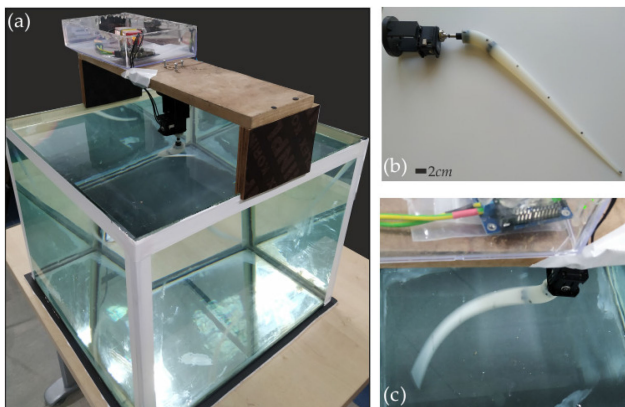
Fig. 7. Static test set-up. A 500-mm long and 500-mm wide tank is used, while the water level is 380 mm. A fixed wood structure is set on top of the tank, with a 3D-printed structure holding the motor. The controlling board and the Li–Po battery are placed in a plastic case on top of the structure.

TABLE II
DRAG AND LIFT COEFFICIENTS [-]

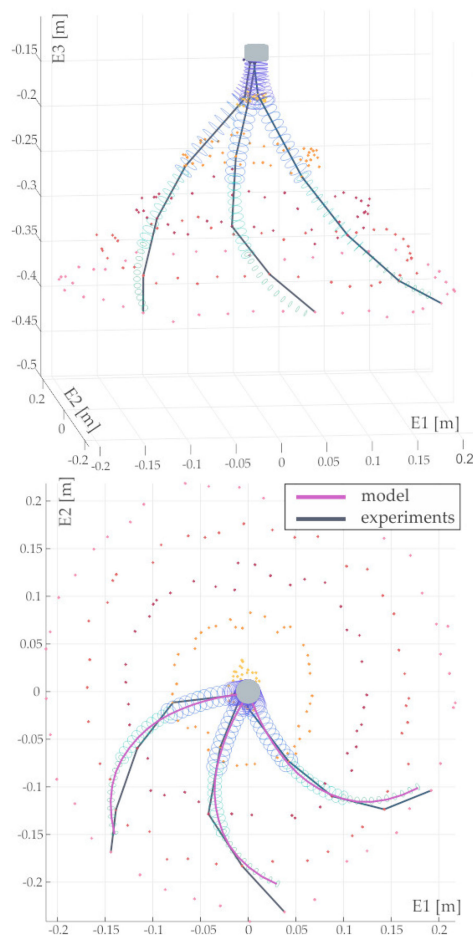| Material		Rotational Speeds			
		ω_1	ω_2	ω_3	ω_4
Dragon Skin™ 30	C_D	1.2	0.8	0.9	0.6
	$-C_L$	0.6	0.1	0.15	0.02
Mold Star™ 30	C_D	1.2	1.1	1.1	1.1
	$-C_L$	0.7	0.5	0.4	0.3
Smooth Sil™ 940	C_D	1.1	1.0	1.3	1.3
	$-C_L$	0.4	0.05	0.05	0.01
ABS (rigid)	C_D	1.1			
	$-C_L$	0.1			

Fig. 8. Comparison between the deformed shapes obtained with the experimental static tests and the theoretical simulations. The graphs present the results obtained with a Smooth-Sil 940 flagellum at a rotational speed $\omega_2 = 0.85\,\omega_{max}$. The red and orange dots represent the position of the six markers placed along the flagellum, depicted from the experiments, while the grey lines are the reconstructed deformed shapes. The theoretical deformed shapes are represented by the blue and green circles, where the three sections used to model the *filament* can be observed. The considered deformed shapes are obtained after five complete loops, to considered only the behaviour of the propeller during the stationary regime, and they are taken 0.2 s apart.

along the *filament*. A direct linear transformation algorithm [33] has been used to obtain the position in space of the markers during the experiment. After calibrating the camera, the videos have been processed to detect the position of the six markers for each frame composing a complete loop of the motor. The tests have been performed at four different speeds: $\omega_{1,2,3,4} = \{0.75, 0.85, 0.95, 1.00\}\omega_{max}$, where $\omega_{max} = 51$ r/min is the maximum speed provided by the MX28-AT motor powered by 11.1 V. Finally, the trials provided the experimental deformed shapes for each module and for each considered rotational speed. For each silicone and rotational speed, a trial and error procedure has been carried out comparing the obtained deformed shapes with those obtained with the theoretical simulation, at varying only the drag and lift coefficients composing matrix (23). More in details, the following fitting procedure is carried out:

1) The dynamical simulations described in Section III are run, using the drag and lift coefficients provided for the rigid case, namely $C_D = 1.1$ and $C_L = -0.1$.
2) The deformed shape obtained from the simulation is compared with the one obtained from the experiment.
3) From the comparison, the coefficients C_D and C_L are increased/decreased and new simulations are run.

The procedure is carried out until the best match between the theoretical and the experimental deformed shapes is obtained (see Fig. 8). The final coefficients that have been found for each silicone and that have been used for all the future simulations are summarized in Table II . For sake of completeness, the

rigid flagellum coefficients, obtained in Section IV-A, are also reported.

It is possible to notice that the lift coefficients C_L obtained for the different materials and speeds are much more variable with respect to the drag ones C_D. This can be explained considering that the lift coefficient depends on the radial speed gradients and it is, therefore, a function of the orientation of the cylinder with respect to the fluid flow. Accordingly, it can vary significantly with the deformed shapes.

Table III presents the percentage errors obtained comparing the position of the six markers obtained thought the experiments and the theoretical model with the estimated C_D and C_L coefficients. The errors are evaluated measuring the difference between the position of the six markers from the experimental trials and the position of the same points obtained from the theoretical model, using the drag and lift coefficients from Table II. Finally, the errors are weighted on the length of the flagellum. Fore sake

TABLE III
MEASURED VERSUS MODELLED MEAN AND TIP POSITION ERRORS [%]

Material		Rotational Speeds			
		ω_1	ω_2	ω_3	ω_4
Dragon Skin™ 30	Mean	5.04	3.37	5.11	6.47
	Tip	9.23	6.98	10.62	10.87
Mold Star™ 30	Mean	5.45	7.51	2.99	4.60
	Tip	13.38	18.12	2.24	8.92
Smooth Sil™ 940	Mean	4.04	3.20	5.70	4.90
	Tip	9.52	4.83	10.53	9.30

of completeness, Table III includes also the errors measured at the tip of the flagellum (i.e., the point where the highest error is measured).

The theoretical simulations provide also the constraint forces and torques exerted at the base during the rotation of the flagellum. Equation (9) represents a mixed dynamic problem, where the forces are known at some generalized coordinates and the accelerations at the rest. In particular, in the static test considered here, the forces are known for the filament and the hook $\tau_f = \tau_h = 0$, the acceleration of the body is such that $q_b = 0$ and the angular acceleration of the motor is set accordingly to the considered rotational speed. Finally, the forces and the torques at the base are obtained as solution to the equations. In total, three torques (m_x, m_y and m_y) and three forces (f_x, f_y, f_z) are obtained and they have been presented in Fig. 9. While all the lateral torques (m_x and m_z) and forces (f_x and f_z) have a null mean during a complete rotation of the motor (represented by dashed lines), this is no longer valid for the out-of-plane torque m_y and force f_y. In particular, the latter represents the total vertical force, which is the resultant between the weight of the flagellum and the thrust that it provides. For the soft flagella, it is possible to notice that, in the transitional regime (the first second), f_y reaches a value that represents the weight of the flagellum. As the motor rotates and the stationary regime is reached, for the soft flagella, the force decreases and thus we can conclude that the net thrust is opposed to the weight, pushing upward the propeller. As the stiffness of the silicone increases, it is possible to notice that this difference increases, so from these results we can expect that the stiffer (soft) flagellum provides the higher positive net thrust. On the other hand, for the rigid module, f_y increases after the transitional regime, so we can presume that the rigid flagellum provides a pulling thrust. This behavior is further discussed and experimentally demonstrated in Section V-A.

V. EXPERIMENTAL TEST ON A SINGLE FLAGELLUM

In this Section, two experimental trials are used to provide a first estimation on the swimming capabilities of the modules. In the first set of trials, the prototype is able to self propel in a marry-go-round set-up. The results have been fundamental to validate the accuracy of the theoretical predictions and to assess the propulsive capacities of the modules, confirming the predictions about the reverse in the thrust direction when going from a soft to a rigid flagellum. In the second trials, a robot prototype, composed by a single flagellar module, has been designed and fabricated.
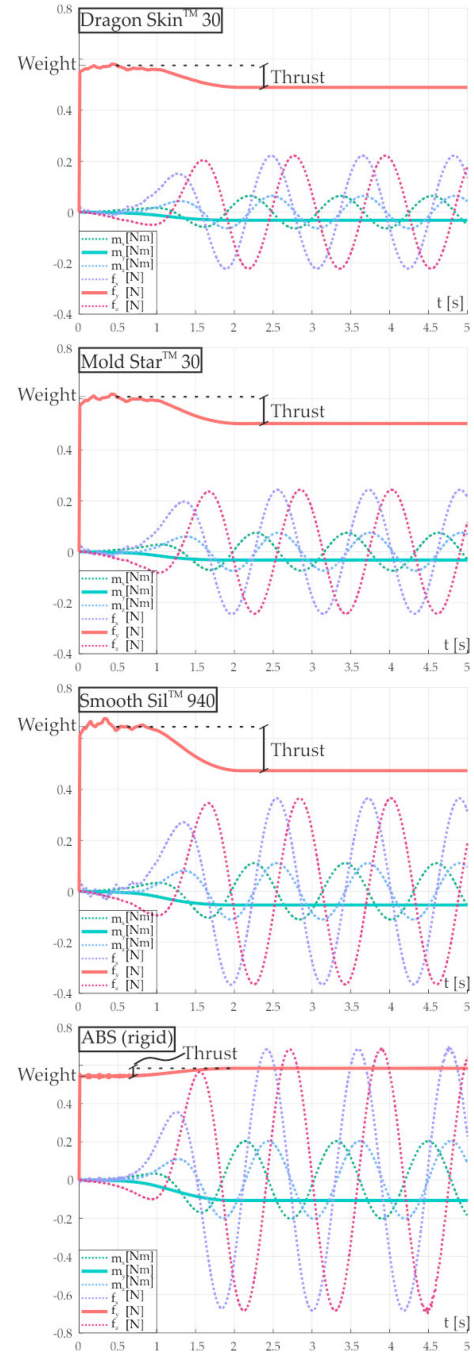

Fig. 9. Constraint torques and forces τ_b exerted at the base, obtained from the theoretical simulations for the four prototypes at the speed $\omega_4 = \omega_{\max}$. It can be noted that only the out-of-plane torque m_y and force f_y have a nonzero mean. In particular, f_y represents the total force given by the net weight of the module in the water and the thrust provided by the flagellum. While for the silicone prototypes the thrust contrasts the weight, for the solid prototype the two forces are summed. Thus, an opposite swimming direction is expected when going from a soft to a rigid flagellum. Moreover, it can be observed that, for the soft modules, the thrust increases with the stiffness of the silicone.

A. Self Propulsion Test

In these trials, the flagellar module is constrained by a passive, fixed stand in a merry-go-round set-up (see Fig. 10). Through a clamp, the waterproof canister containing the actuating motor is held by a passive arm, which is connected to the fixed stand
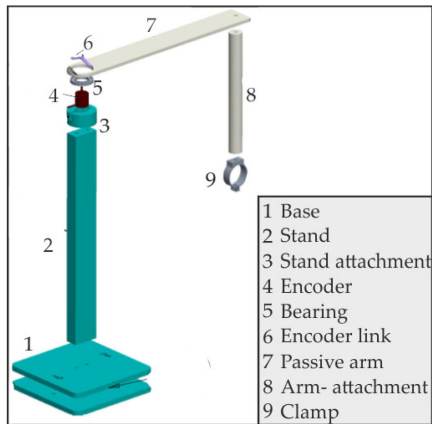
Fig. 10. Design of the set-up for the self propulsive test, where a marry-go-round motion is realized. A fixed stand is connected, through two passive arms, to a clamp required to hold the waterproof canister enclosing the actuating motor. A rotary encoder, placed inside the stand, measures the rotational speeds of the arm. Bearing are used to reduce effect of friction.
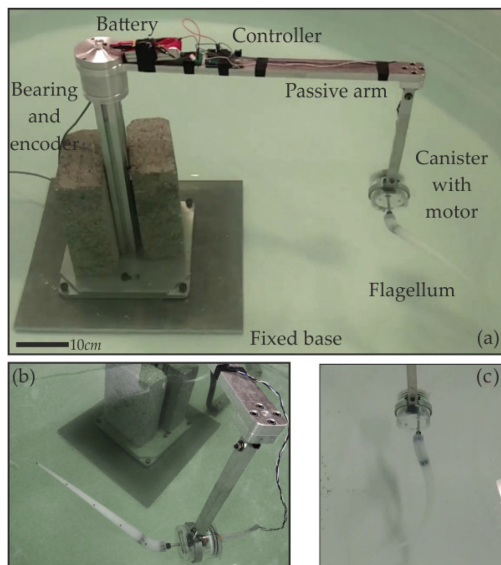

Fig. 11. Self propulsive set-up, with the canister connected to the flagellum. The motor is connected to an Arbotix-M Robocontroller which is wirelessly controlled by an X-Bee module. Both the board and the motor are powered by a 11.1 V, 2200 mAh Li–po battery. The board and battery are placed on the passive arm.

containing a 1024 P/R (Quadrature) rotary encoder. Bearings are used to ensure friction-less rotation of the arm. In this case, the Arbotix-M Robocontroller and the Li–Po battery used to control and power the motor are placed on top of the passive arm (see Fig. 11). The thrust provided by the onset of helical waves along the filament is converted in the rotation of the passive arm around the fixed stand. Using an Arduino Mega connected to a laptop, the rotary encoder is employed to read the rotational speed and to relate the propulsive capability of the flagellar modules to their material stiffness and to the speed provided by the actuation motors.

The trials have been performed at the same four different speeds used for the statics tests in Section IV-B, both clockwise and counter-clockwise, for 4 min. The swimming speeds
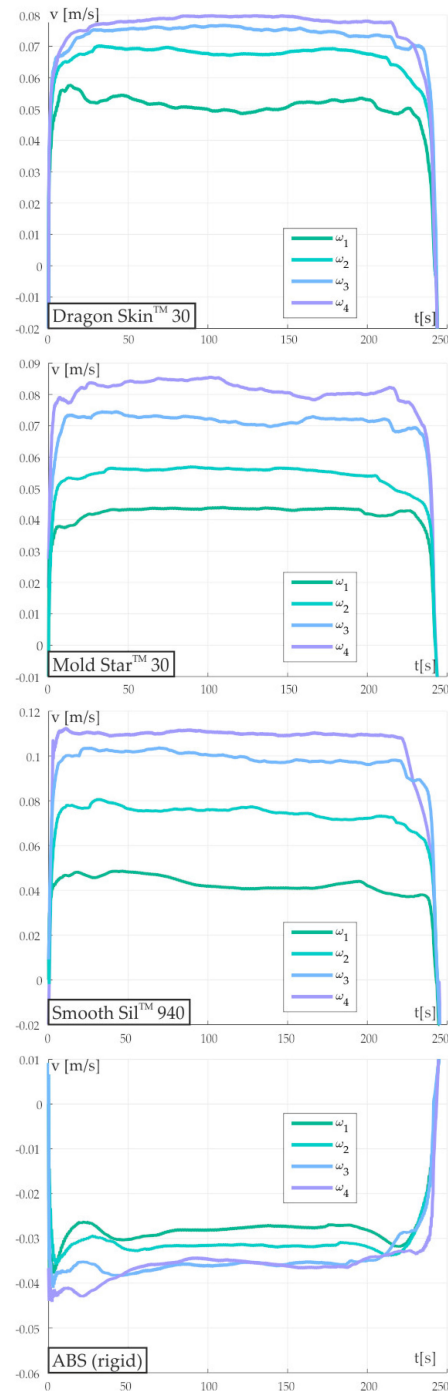

Fig. 12. Experimental results from the self propulsive test. The graphs present the rotational speed measured by the rotary encoder, for four motors speeds $\omega_{1,\ldots,4} = \{0.75, 0.85, 0.95, 1.00\}\omega_{\max}$, where $\omega_{\max} = 51$ r/min. In particular, it should be noted that the speeds recorded for the rigid ABS flagellum are opposite in sign, since the rigid design provides a negative (pulling) thrust. These results confirm the prediction of the theoretical modeling presented. The mean values of the speeds are reported in Table IV.

obtained during these tests are reported in Fig. 12. Finally, the results have been compared to those predicted by the theoretical model, in order to validate its accuracy. Table IV presents the swimming speeds obtained both in the experimental tests and through the model.

TABLE IV
SWIMMING SPEEDS [M/S]

Material		Rotational speeds			
		ω_1	ω_2	ω_3	ω_4
Dragon Skin™ 30	Exp.	0.051	0.067	0.075	0.074
	Model	0.050	0.067	0.076	0.074
Mold Star™ 30	Exp	0.043	0.055	0.071	0.081
	Model	0.045	0.058	0.071	0.080
Smooth Sil™ 940	Exp.	0.043	0.074	0.098	0.107
	Model	0.042	0.076	0.096	0.103
ABS	Exp.	−0.028	−0.031	−0.035	−0.036
	Model	−0.027	−0.031	−0.034	−0.036

It can be noted that:

1) at the lowest motor's speed, $\omega_1 = 0.75\,\omega_{\max}$, the Dragon Skin™30 silicone, namely the softest one, provides the highest swimming speed;

2) at the highest motor's speed, $\omega_4 = \omega_{\max}$, the Smooth-Sil™940 silicone, namely the stiffer one (excluding the rigid flagellum) provides the highest swimming speed;

3) at all motor's speeds, the rigid flagellum provides a negative thrust which, instead of pushing forward the arm, pulls it, resulting in a swim in the opposite direction with respect to the deformable modules.

In particular, the change in the direction of the thrust when going from a soft to a rigid propeller proves once again the relevance of elasticity and the complete opposite results that can be obtained using deformable materials. In particular, the drag and the lift forces are directed, respectively, perpendicular and parallel to the direction of the flow with respect to the cross section of the propeller. In the rigid case, these directions are constant along the length of the flagellum and their inclination is set by the precurvature of the hook, which, in our design, is equal to $45°$. On the other side, as a consequence of the interaction with the fluid, the soft flagella are highly deformed, resembling an helical shape whose properties depends on the stiffness of the material and on the rotational speed of the motor. For this reason, the direction of the fluid flow with respect to the cross section varies along the length of the flagellum, thus different directions of the drag and lift forces are observed, finally providing a reversion in the resultant thrust force with respect to the rigid case. Ideally, a limit value of the stiffness of the module could be found, where the change in the direction of the thrust is realized. This will be subject of further investigation on a future work. In conclusion, the obtained results prove that the theoretical model is capable of precisely predicting the behavior and, in particular, the thrust provided by the modules (both rigid and soft). Moreover, the swimming capabilities of the flagellar propellers have been proved, paving the way to the design and fabrication of a new family of robots that rely on these modules to self propel.

B. Single Flagellum Prototype

In this section, a robot prototype, composed by a single flagellar module, is designed and fabricated. The same waterproof canister employed in the self propulsion test is now used to contain the MX28-AT motor. The robot is tethered through particularly flexible and long wires, which are connected to the
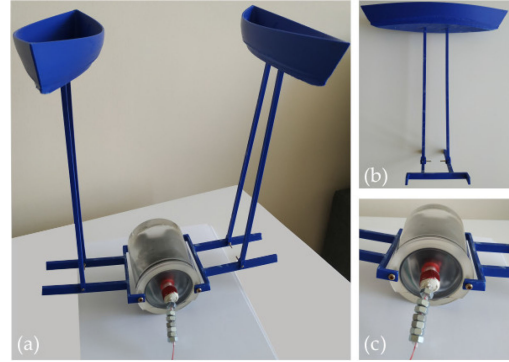

Fig. 13. Single module prototype. The motor is contained inside the waterproof acrylic canister (c), while a system of hull structures have been designed and 3D-printed (b) to constrain the reaction torque.

Li-Po battery and the Arbotix board placed outside the pool. The free swimming of the robot has been tested in a 2-m wide and 4 m long pool, with a water level depth of 60 cm. Using a single module, particular attention needs to be paid to constrain the rotations of the canister that are caused by the motor torque. In fact, in Section IV-B (see Fig. 9), it has been showed that only two reaction forces are not null during the rotation of the single flagellum: the propulsive thrust f_y and the out-of-plane torque m_y. Bacterial flagella employ a counter-rotation of the head to compensate the screw rotation of the tail, resulting in total torque balance. For the sake of simplicity, in the proposed prototype, a system of boat hull structures has been designed and 3D-printed using ABS in order to constrain the out-of-plane torque m_y. In particular, the structure is composed of two canoe-boats and a system of beams which are finally tightened to the canister. The submerged part of the hull structure naturally adapts to the motion of the prototype, assuring the required rotational constraint to the canister for the entire time of the motion. Finally, some weights have been placed on one end of the canister to assure the full submersion of the vehicle. The motor has been powered at its maximum speed $\omega_4 = 51$ r/min. Some snapshots of the vehicle during an experiment are reported in Fig. 14. A straight motion is obtained, with an average swimming speed of 2.5 cm/s. It should be noted that the considered silicone, in the self-propulsive set-up in Section V-A, presented a swimming speed around 1 cm/s (see Table IV). The lower swimming speed is mostly due to the presence of the passive arm that is also pushed by the propeller, while in the single flagellum prototype only the canister is added.

VI. FLAGELLATE VEHICLE

A completely untethered vehicle, equipped with four flagella, has been designed, fabricated and tested (see Fig. 15). An aluminium shell is designed to contain the motors, the battery and all the required electronic components. The shell is divided in two elongated domes having a diameter of 180 mm each, which are joined using rubber O-rings and screws to obtain a total length of 210 mm. The first dome contains an ABS 3D-printed structure supporting the four motors which, through 4 mm holes sealed with O-rings, are connected to the flagellar modules outside the
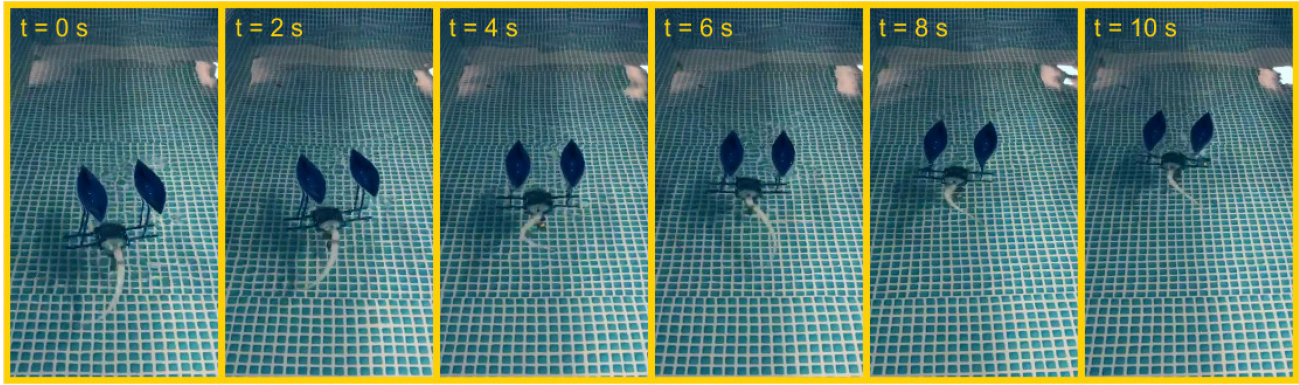
Fig. 14.   Snapshots taken during an experiment with the single module prototype. Here, a flagellar module made with Dragon Skin 30 silicone has been used.
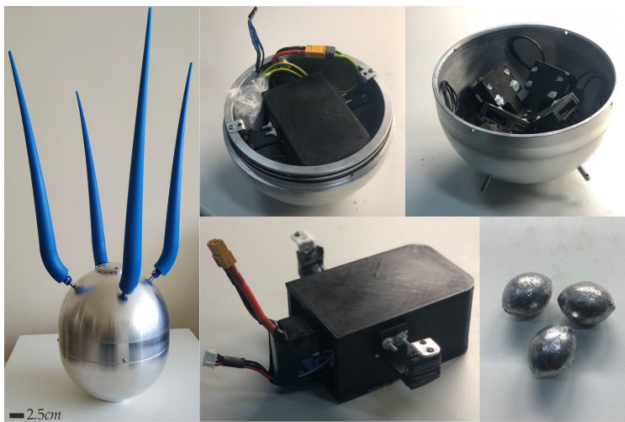

Fig. 15.   Four-modules vehicle, composed by an aluminium shell and four flagellar propellers made with Mold Star^{TM}30 silicone. Details of the shell's interiors, with the 3D-printed case containing the Li–Po battery and the board and the structure with the four motors are shown. Some weights were used to balance the whole structure in the water.
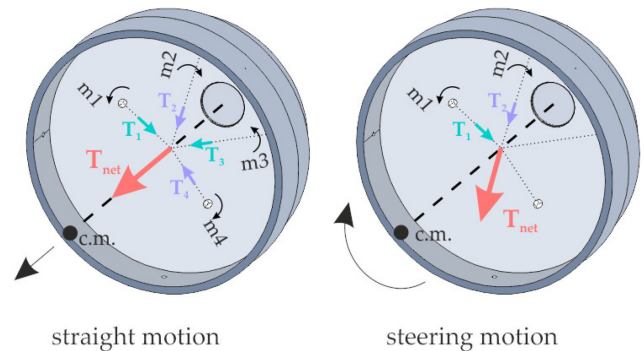

Fig. 16.   Design of the aluminium shell for the four-modules vehicle. The position of the motors has been specifically determined in order to sum the thrusts provided by the four flagella and, at the same time, to prevent any entanglement. To obtain a straight motion, all the four motors are run at the same angular speed, with opposite directions. For a steering motion, only to motors are run, with opposite direction. In the Figure, c.m. represents the center of mass of the vehicle.

shell. The second dome contains the Arbotix-M robocontroller and the Li–Po battery, which is placed inside a 3D-printed ABS box secured to dome's walls to prevent any damage to the electronic components during the motion of the vehicle. A magnetic sensor is connected to the Arbotix-M Robocontroller to launch the motor's rotation. Finally, some weights have been placed to compensate the buoyancy due to the air trapped and to obtain a straight at-rest position of the vehicle in the water. In this case, the four flagellar modules are made out of Mold Star 30 silicone.

The position of the four motors on the shell has been analyzed in order to obtain the maximum thrust preventing, at the same time, any possible entanglement between the flagella(see Fig. 16). For this reason, they are positioned resembling the configuration of the propellers on a quadrotor systems and with an inclination angle of $45°$ with respect to the center line of the dome. Moreover, opposite flagella present a $180°$ phase shift in their at-rest position and they also rotate with alternate directions. In this way, the out-of-plane reaction torque, which was compensated by the hull structures for the single module prototype in Section V-B, now automatically vanishes as a

combination of the opposite reactions provided by each flagella. The theoretical model presented in Section III is employed to first estimate the performance of the designed vehicle and to investigate the motors speeds to obtain different swimming modes. The model is expanded to consider the presence of four propellers and the rigid body is modeled to represent the geometry of the shell and the weight that it contains. In particular, as mentioned in Section III-A, it is crucial to precisely calculate the distribution of the mass inside the shell in order to correctly model the distance between the center of gravity and the center of buoyancy. In the considered case, the total inertia matrix of the canister in (16) is given by the shell's inertia, the battery with its case, the Arbotix-M Robocontroller, the weights that were used to balance the structure in the water and the four motors with the structure holding them. In this way, from (17) it was possible to observe that the center of gravity c of the canister is positioned toward the front part of the vehicle. Considering the presence of the flagella, which are positioned on the back of the vehicle, the center of the mass of the entire vehicle is thus positioned in its geometrical center, which is also the center of buoyancy, ensuring the stability of the system and preventing unintended rotation.
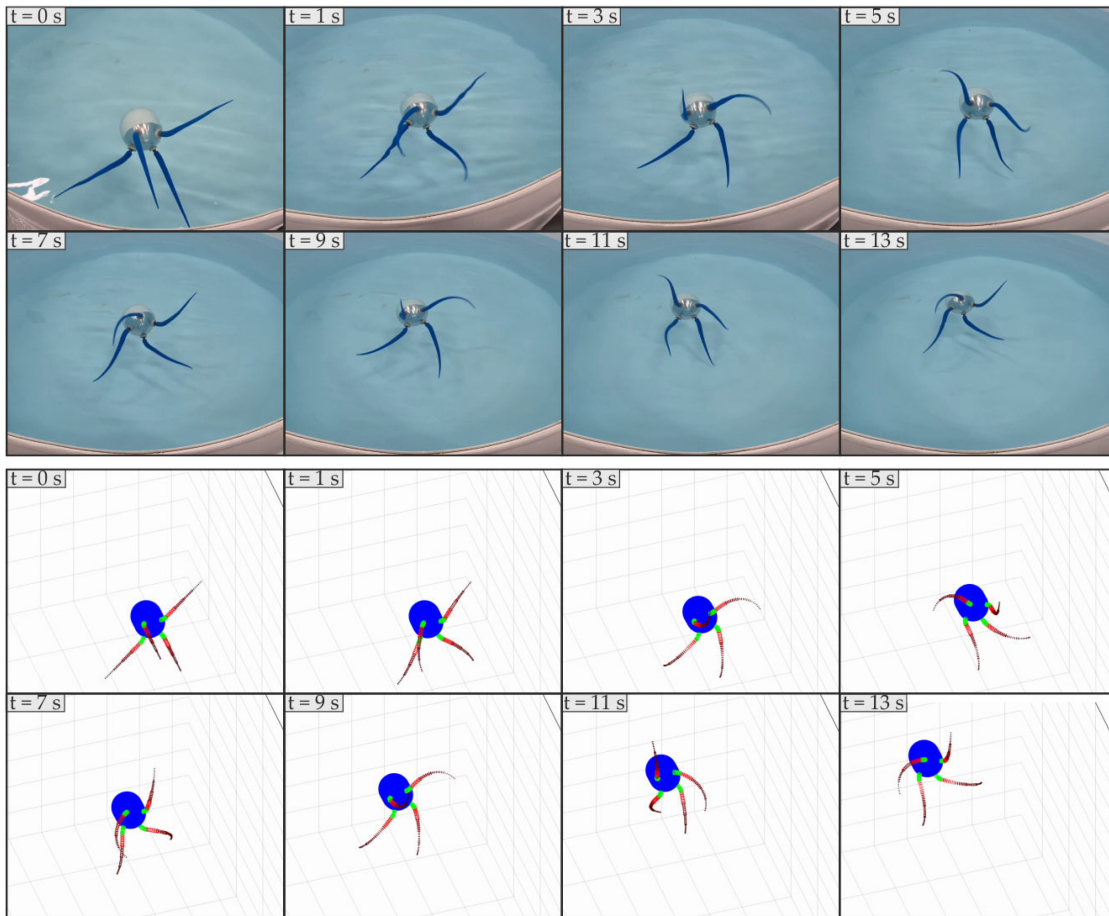
Fig. 17. Snapshots taken from the video of an experiment with the four flagella robot moving straight. At rest, $t = 0$ s, the modules start from a configuration with opposite phases. Once the magnet sensor is activated, $t = 1$ s, the motors start rotating in opposite directions and a straight motion is obtained.

A. Straight Motion

In order to obtain a straight motion, the simulations are run with the four motors rotating at the maximum speed, with alternate directions. The results of the simulations are presented in Fig. 17, where some snapshots of the simulations are presented and compared with the results of the experiments performed with the same specifications. At $t = 0$, it is possible to notice the initial configuration, with two modules in a straight position, while the opposite two present a $180°$ phase shift. The motors then start rotating with alternate directions and the steering straight motion is attained. After 13 s, the robot travelled 70 cm, with an average swimming speed of 5.38 cm/s. The power consumption of the prototypes is mostly related to the consumption of the motors, which is around 22 W. The complete video of both the simulation and the experiment are contained in the supplementary material. In this regard, the proposed theoretical model represents a useful tool to efficiently investigate the behavior of different designs and geometries of both the propellers and the vehicle.

B. Steering Motion

Following the approach for the flight control of quadrotor systems, in order to obtain a steering motion, two motors are run at the maximum speed, with alternate directions, while the other two are held stationary. Since, as explained above, the center of mass is positioned front with respect to the flagella, the vehicle rotates on the side of the two rotating propellers. The results of the simulations are presented in Fig. 18, where some snapshots of the simulations are presented and compared with the results of the experiments performed with the same specifications. The modeled and the experimental prototype present very similar behavior until a complete $90°$ rotation is obtained. Going on, while the modeled vehicle continues rotating with a trajectory resembling a circle, the real vehicle presents an ellipsoid-like trajectory. This discrepancy is due to the fact that the vehicle is slightly negatively buoyant (a perfect neutral buoyancy is very difficult to obtain with the proposed design) and the experiments are run in a relatively small tank, where the flagella brush up against the tank's bottom. In a future research, an improved version of the vehicle will be investigated and the experiments will be performed in a real pool. This prototype represents a first example of one of the many solutions that could be obtained employing the flagellar modules as propulsive source. Different designs and results can be attained optimizing the position, the number, the material and the design of the modules, possibly resulting in increased overall performances of the robot.
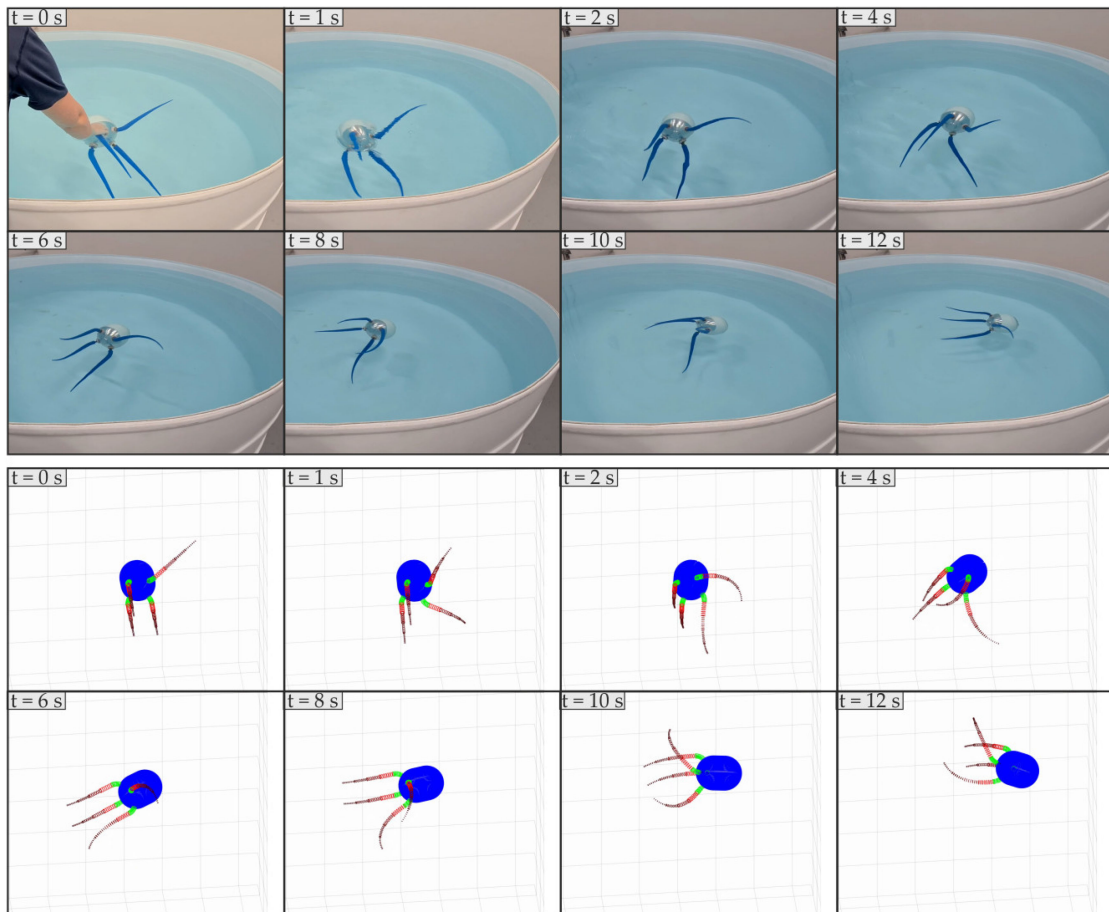
Fig. 18.   Snapshots taken from the video of an experiment with the four flagella robot performing a steering motion. At rest, $t = 0$ s, the two rotating modules start from a configuration with opposite phases, while the two resting propellers are kept straight to reduce their interference with the motion. Once the magnet sensor is activated, $t = 1$ s, the two motors start rotating in opposite directions and a steering motion is obtained.

VII. CONCLUSION

In this article, we introduced a new family of soft propellers, inspired by prokaryotic bacteria flagellum. After tackling the bioinspired design, a geometrical model was presented to investigate the dynamics and, in particular, the swimming capabilities of the proposed design. The model was refined and validated by two sets of trials on the single flagellum, while a complete vehicle was designed and fabricated to prove the feasibility of the proposed approach for the fabrication of new solutions for underwater robotics. Some interesting results were found in particular when employing different materials to fabricate the modules, obtaining complete opposite behavior when going from a soft to a rigid module. In a future work, a new, improved prototype will be designed and fabricated, combining the action of a greater number of modules with different designs and materials. Onboard sensors will be used to gain information to improve both the performance of the vehicle and the theoretical predictions, in particular the hydro-dynamical model. These results paved the way to the investigation of optimal stiffness and materials that can be employed depending on the final solution that is searched for. Our modules resemble those encountered in nature, but a great number of different design and solution can be

obtained at varying the material, the geometry, the dimensions of the modules. Within this context, the theoretical model offered a precise and computationally efficient strategy to investigate the behaviors of each design. In particular, an optimization procedure can be carried out, with the purpose to maximize the efficiency of the system, rather than its velocity. Moreover, the soft modules can be designed in order to provide them with grasping capabilities, taking advantage of their elongated shape. The soft material employed for the proposed propeller allows the tackling of challenges that are hardly dealt with by traditional rigid technologies, especially while interacting with unstructured environment. In particular, the high degree of compliance and the low risk of damage from impact of the soft underwater propellers, offered the chance of unprecedented proximity in surveillance and monitoring operations (as for the surveillance of off-shore structures or for the monitoring of aquatic species). The flexibility and adaptability of the robot structure, as well as the possibility of physically interacting with the surrounding, ensured a safer and more efficient operation in a cluttered environment, drastically reducing the entanglement problem. These features, coupled with peculiar noiseless locomotion, make this kind of robots suitable for a broad range of

tasks currently unsolved, such as the noninvasive monitoring of water quality and marine habitats, easing the mapping of the species and their distribution.

APPENDIX A
NOMENCLATURE

$\tilde{\boldsymbol{\nu}} = \begin{pmatrix} 0 & -\nu_3 & \nu_2 \\ \nu_3 & 0 & -\nu_1 \\ -\nu_2 & \nu_1 & 0 \end{pmatrix}$ isomorphism between 3-D vectors $\boldsymbol{\nu} = (\nu_1, \ \nu_2, \ \nu_3) \in \mathbb{R}^3$ and skew symmetric matrices $\mathfrak{so}(3)$.

$e^{X\widehat{\boldsymbol{\xi}}} = \boldsymbol{I}_4 + X\widehat{\boldsymbol{\xi}} + \frac{1}{\theta^2}(1 - \cos(X\theta))\widehat{\boldsymbol{\xi}}^2 + \frac{1}{\theta^3}(X\theta - \sin(X\theta))\widehat{\boldsymbol{\xi}}^3$, exponential map with $\theta^2 = \mathsf{k}^T\mathsf{k}$.

$\mathrm{ad}_{\boldsymbol{\xi}} \ (X) = \begin{pmatrix} \widetilde{\mathsf{k}} & \boldsymbol{0}_{3\times3} \\ \widetilde{\mathsf{p}} & \widetilde{\mathsf{k}} \end{pmatrix} \in \mathbb{R}^{6\times6}$

$\mathrm{ad}_{\boldsymbol{\eta}} \ (X) = \begin{pmatrix} \widetilde{\mathsf{w}} & \boldsymbol{0}_{3\times3} \\ \widetilde{\mathsf{v}} & \widetilde{\mathsf{w}} \end{pmatrix} \in \mathbb{R}^{6\times6}$ adjoint representation of the strain and twist vectors.

$\mathrm{ad}_{\boldsymbol{\xi}}^* \ (X) = \begin{pmatrix} \widetilde{\mathsf{k}} & \widetilde{\mathsf{p}} \\ \boldsymbol{0}_{3\times3} & \widetilde{\mathsf{k}} \end{pmatrix} \in \mathbb{R}^{6\times6}$

$\mathrm{ad}_{\boldsymbol{\eta}}^* \ (X) = \begin{pmatrix} \widetilde{\mathsf{w}} & \widetilde{\mathsf{v}} \\ \boldsymbol{0}_{3\times3} & \widetilde{\mathsf{w}} \end{pmatrix} \in \mathbb{R}^{6\times6}$ coadjoint representation of the strain and twist vectors.

$\mathrm{Ad}_{\boldsymbol{g}} \ (X) = \begin{pmatrix} \boldsymbol{R} & \boldsymbol{0}_{3\times3} \\ \widetilde{\mathsf{u}}\boldsymbol{R} & \boldsymbol{R} \end{pmatrix} \in \mathbb{R}^{6\times6}$. Adjoint representation of SE(3).

$\mathrm{Ad}_{\boldsymbol{g}}^* \ (X) = \begin{pmatrix} \boldsymbol{R} & \widetilde{\mathsf{u}}\boldsymbol{R} \\ \boldsymbol{0}_{3\times3} & \boldsymbol{R} \end{pmatrix} \in \mathbb{R}^{6\times6}$ coAdjoint representation of SE(3).

$\mathrm{T}_{\boldsymbol{\xi}} \ (X) = \int_0^X \mathrm{Ad}_{\boldsymbol{g}(s)} ds \in \mathbb{R}^{6\times6}$ tangent operator of the exponential map.

APPENDIX
B DERIVATION OF THE GENERALIZED DYNAMIC EQUATIONS FOR THE HYBRID SYSTEM

The dynamic equation of motion for the considered hybrid system could be obtained by a direct application of the Lagrange equations. However, this would require the calculation of the mass matrix Christoffel symbols and it would lead to a messy expression. For this reason, we employ an equivalent derivation based on the D'Alembert's principle and on the momentum balance, which was presented in [22] and [23]. The main steps are also presented here for sake of completeness.

A. Rigid Bodies

Let us consider a virtual displacement $\delta\boldsymbol{\zeta}_i \in \mathbb{R}^6$, which satisfies the condition $\delta\boldsymbol{\zeta}_i = \boldsymbol{J}_i\delta\boldsymbol{q}$. The equation of motion (6) is then projected onto the linear space generated by $\delta\boldsymbol{\zeta}_i^T = \delta\boldsymbol{q}^T\boldsymbol{J}_i^T$

$$\delta\boldsymbol{q}^T \left\{ \boldsymbol{J}_i^T \left[\boldsymbol{\mathcal{M}}_i \left(\boldsymbol{J}_i\ddot{\boldsymbol{q}} + \dot{\boldsymbol{J}}_i\dot{\boldsymbol{q}} \right) + ad_{\boldsymbol{\eta}_i}^* \left(\boldsymbol{\mathcal{M}}_i\boldsymbol{J}_i\dot{\boldsymbol{q}} \right) \right] \right. \tag{31}$$
$$\left. - \boldsymbol{J}_i^T \left(\boldsymbol{\mathcal{F}}_{J_i} - Ad_{\boldsymbol{g}_{ij}\boldsymbol{g}_j}^* \boldsymbol{\mathcal{F}}_{J_j} \right) - \boldsymbol{J}_i^T\boldsymbol{\mathcal{F}}_{e_i} \right\} = 0$$

which should be satisfied $\forall\delta\boldsymbol{q} \in \mathbb{R}^n$, leading to the generalized dynamic equations

$$\left(\boldsymbol{J}_i^T\boldsymbol{\mathcal{M}}_i\boldsymbol{J}_i \right)\ddot{\boldsymbol{q}} + \boldsymbol{J}_i^T \left(ad_{\boldsymbol{\eta}_i}^*\boldsymbol{\mathcal{M}}_i\boldsymbol{J}_i + \boldsymbol{\mathcal{M}}_i\dot{\boldsymbol{J}}_i \right)\dot{\boldsymbol{q}} = \tag{32}$$
$$\boldsymbol{J}_i^T \left(\boldsymbol{\mathcal{F}}_{J_i} - Ad_{\boldsymbol{g}_{ij}\boldsymbol{g}_j}^* \boldsymbol{\mathcal{F}}_{J_j} + \boldsymbol{J}_i^T\boldsymbol{\mathcal{F}}_{e_i} \right) \ .$$

B. Soft Bodies

Let us consider a virtual displacement field $\delta\boldsymbol{\zeta}_i(\cdot)$, which satisfies the condition $\delta\boldsymbol{\zeta}_i(X) = \boldsymbol{J}_i(X)\delta\boldsymbol{q} \in \mathbb{R}^6$. Following the same procedure employed for the rigid case, the following generalized dynamic equations are obtained:

$$\left(\int_0^{L_i} \boldsymbol{J}_i^T\bar{\boldsymbol{\mathcal{M}}}_i\boldsymbol{J}_i dX_i \right)\ddot{\boldsymbol{q}}$$
$$+ \left(\int_0^{L_i} \boldsymbol{J}_i^T \left(ad_{\boldsymbol{\eta}_i}^*\bar{\boldsymbol{\mathcal{M}}}_i\boldsymbol{J}_i + \bar{\boldsymbol{\mathcal{M}}}_i\dot{\boldsymbol{J}}_i \right) dX_i \right)\dot{\boldsymbol{q}} = \tag{33}$$
$$\int_0^{L_i} \boldsymbol{J}_i^T \left(\boldsymbol{\mathcal{F}}_{i_i}' + ad_{\boldsymbol{\xi}_i}^*\boldsymbol{\mathcal{F}}_{i_i} \right) dX + \int_0^{L_i} \boldsymbol{J}_i^T\bar{\boldsymbol{\mathcal{F}}}_{e_i} dX_i \ .$$

C. Soft-Rigid Multibody

The virtual work of the whole multibody system is the sum of the virtual work of each subsystem. Thus, the equation of motion for the soft-rigid multibody system is composed by the sum of equations like (32) and (33) over all the bodies of the system. This operation yields to the generalized dynamic equations in the classical form (9). In particular, the internal elastic force takes the form

$$\boldsymbol{\tau}_i = \sum_{j=i}^{N} \int_0^{L_j} {}^j\boldsymbol{S}_i^T \left(\boldsymbol{\mathcal{F}}_{i_j}' + ad_{\boldsymbol{\xi}_j}^*\boldsymbol{\mathcal{F}}_{i_j} \right) dX_j \tag{34}$$

where by definition, ${}^j\boldsymbol{S}_i = \boldsymbol{0}$ for $j < i$. The first integral of the series can be analytically solved by integration by part considering the identity $T_{\boldsymbol{\xi}}^{T'} = Ad_{\boldsymbol{g}}^T = Ad_{\boldsymbol{g}^{-1}}^*$, while all the other integrals can be analytically solved considering the identity $Ad_{\boldsymbol{g}}^*(\boldsymbol{\mathcal{F}}' + ad_{\boldsymbol{\xi}}\boldsymbol{\mathcal{F}}) = (Ad_{\boldsymbol{g}}^*\boldsymbol{\mathcal{F}})'$. In this way, it is possible to obtain the internal elastic load for the section ith as follows:

$$\boldsymbol{\tau}_i = \sum_{j=i}^{N} ({}^j\boldsymbol{S}_i^T\boldsymbol{\mathcal{F}}_{i_j})|_0^{L_j} - \boldsymbol{B}_i^T \int_0^{L_i} \boldsymbol{\mathcal{F}}_{i_i} dX_i. \tag{35}$$

Finally, imposing the boundary conditions (7) and the constitutive law (8), yields to the stiffness matrix of the system

$$\boldsymbol{\tau}_i = -\boldsymbol{B}_i^T \int_0^{L_i} \boldsymbol{\Sigma}_i dX_i \boldsymbol{B}_i^T \boldsymbol{q}_i \tag{36}$$

REFERENCES

[1] A. D. Marchese, D. Onal Cagdas, and D. Rus, "Autonomous soft robotic fish capable of escape maneuvers using fluidic elastomer actuators," *Soft Robot.*, vol. 1, no. 1, pp. 75–673, Mar. 2014.

[2] M. Calisti, G. Picardi, and C. Laschi, "Fundamentals of soft robot locomotion," *J. Roy. Soc. Interface*, vol. 14, no. 130, pp. 20170101, 2017.

[3] F. Giorgio-Serchi, A. K. Lidtke, and G. D. Weymouth, "A soft aquatic actuator for unsteady peak power amplification," *IEEE/ASME Trans. Mechatronics*, vol. 23, no. 6, pp. 2968–2973, Dec. 2018.

[4] F. Renda, F. Giorgio-Serchi, F. Boyer, C. Laschi, J. Dias, and L. Seneviratne, "A unified multi-soft-body dynamic model for underwater soft robots," *Int. J. Robot. Res.*, vol. 37, no. 6, pp. 648–666, 2018.

[5] C. Stefanini *et al.*, "A novel autonomous, bioinspired swimming robot developed by neuroscientists and bioengineers," *Bioinspiration Biomimetics*, vol. 7, no. 2, May 2012, Art. no. 25001.

[6] L. Manfredi *et al.*, "A bioinspired autonomous swimming robot as a tool for studying goal-directed locomotion," *Biol. Cybern.*, vol. 107, no. 5, pp. 513–527, 2013.

[7] S. J. Park *et al.*, "Phototactic guidance of a tissue-engineered soft-robotic ray." *Science*, vol. 353,6295, no. 2016, pp. 158–162, 2016.

[8] M. Rossi, G. Cicconofri, A. Beran, G. Noselli, and A. DeSimone, "Kinematics of flagellar swimming in euglena gracilis: Helical trajectories and flagellar shapes," *Proc. Nat. Acad. Sci.*, vol. 114, no. 50, pp. 13085–13090, 2017.

[9] G. Noselli, A. Beran, M. Arroyo, and A. DeSimone, "Swimming euglena respond to confinement with a behavioural change enabling effective crawling." *Nat. Phys.*, vol. 15, no. 50, pp. 496–502, 2019.

[10] M. LaBarbera, "Why the wheels won't go," *Amer. Naturalist*, vol. 121, no. 3, pp. 395–408, 1983.

[11] J. Singleton, E. Diller, T. Andersen, S. Regnier, and M. Sitti, "Micro-scale propulsion using multiple flexible artificial flagella," in *Proc. IEEE/RSJ Int. Conf. Intell. Robots Syst.*, 2011, pp. 1687–1692.

[12] W. Gao, S. Sattayasamitsathit, K. M. Manesh, D. Weihs, and J. Wang, "Magnetically powered flexible metal nanowire motors." *J. Amer. Chem. Soc.*, vol. 132, no. 41, pp. 14 403–14 405, 2010.

[13] T. S. Yu, E. Lauga, and A. E. Hosoi, "Experimental investigations of elastic tail propulsion at low reynolds number," *Phys. Fluids*, vol. 18, no. 9, 2006, Art. no. 91701.

[14] M. Calisti *et al.*, "Design, modeling and testing of a flagellum-inspired soft underwater propeller exploiting passive elasticity," in *Proc. IEEE/RSJ Int. Conf. Intell. Robots Syst.*, 2019, pp. 3328–3334.

[15] Y. Park, Y. Kim, and S. Lim, "Locomotion of a single-flagellated bacterium," *J. Fluid Mech.*, vol. 859, pp. 586–612, 2019.

[16] R. D. Allen and P. Baumann, "Structure and arrangement of flagella in species of the genus beneckea and photobacterium fischeri," *J. Bacteriol.*, vol. 107, no. 1, pp. 295–302, 1971.

[17] L. Koens, H. Zhang, M. Moeller, A. Mourran, and E. Lauga, "The swimming of a deforming helix," *Eur. Phys. J. E*, vol. 41, no. 10, Oct. 2018, Art. no. 119.

[18] F. Samatey *et al.*, "Structure of the bacterial flagellar hook and implication for the molecular universal joint mechanism," *Nature*, vol. 431, pp. 1062–1068, 2004.

[19] F. A. Samatey *et al.*, "Structure of the bacterial flagellar protofilament and implications for a switch for supercoiling," *Nature*, vol. 410, pp. 331–337, 2001.

[20] D. DeRosier, "The turn of the screw: The bacterial flagellar motor," *Cell*, vol. 93, no. 1, pp. 17–20, 1998.

[21] H. Shum and E. A. Gaffney, "The effects of flagellar hook compliance on motility of monotrichous bacteria: A modeling study," *Phys. Fluids*, vol. 24, no. 6, 2012, Art. no. 061901.

[22] F. Renda, F. Boyer, J. Dias, and L. Seneviratne, "Discrete cosserat approach for multisection soft manipulator dynamics," *IEEE Trans. Robot.*, vol. 34, no. 6, pp. 1518–1533, Dec. 2018.

[23] F. Renda and L. Seneviratne, "A geometric and unified approach for modeling soft-rigid multi-body systems with lumped and distributed degrees of freedom," in *Proc. IEEE Int. Conf. Robot. Automat.*, 2018, pp. 1567–1574.

[24] R. W. Brockett, "Robotic manipulators and the product of exponentials formula," in *Proc. Math. Theory Netw. Syst*. SpringerBerlin Heidelberg, 1984, pp. 120–129.

[25] F. Boyer and F. Renda, "Poincare's equations for cosserat media: Application to shells," *J. Nonlinear Sci.*, vol. 27, pp. 1–44, 2016.

[26] F. Renda, V. Cacucciolo, J. Dias, and L. Seneviratne, "Discrete cosserat approach for soft robot dynamics: A new piece-wise constant strain model with torsion and shears," in *Proc. IEEE/RSJ Int. Conf. Intell. Robots Syst.*, 2016, pp. 5495–5502.

[27] J. Selig, *Geometric Fundamentals of Robotics, Ser. Monographs in Computer Science*. New York, NY, USA: Springer, 2007.

[28] M. Piñeirua, R. Godoy-Diana, and B. Thiria, "Resistive thrust production can be as crucial as added mass mechanisms for inertial undulatory swimmers." *Phys. Rev. E., Stat., Nonlinear, Soft Matter Phys.*, vol. 92 2, 2015, Art. no. 021001.

[29] T. I. Fossen, *Guidance and Control of Ocean Vehicles*. New York, NY, USA: Wiley, 1994.

[30] F. Boyer, M. Porez, and A. Leroyer, "Poincare cosserat equations for the lighthill three-dimensional large amplitude elongated body theory: Application to robotics," *J. Nonlinear Sci.*, vol. 20, no. 1, pp. 47–79, 2010.

[31] R. Featherstone, *Rigid Body Dynamics Algorithms*. New York, NY, USA: Springer, 2008.

[32] B. R. Munson and D. Young, *Fundamental of Fluid Mechanics*. Hoboken, NJ, USA: Wiley, 2006.

[33] T. L. Hedrick, "Software techniques for two-and three-dimensional kinematic measurements of biological and biomimetic systems," *Bioinspiration Biomimetics*, vol. 3, no. 3, 2008, Art. no. 034001.

Costanza Armanini (Associate Member, IEEE) received the B.Sc. and M.Sc. degrees in civil engineering from the University of Trento, Italy, in 2011 and 2014, respectively, and the Ph.D. degree in civil, environmental, and mechanical engineering degree from the University of Trento, Italy, in 2018.

She is currently a Post doctoral Fellow with the Department of Mechanical Engineering, Khalifa University, Abu Dhabi, UAE. Her research interests include the modeling of bodies undergoing large deflections and the harnessing of the involved instabilities and nonlinearities for the development of novel technologies, with a special focus on soft robotics applications.
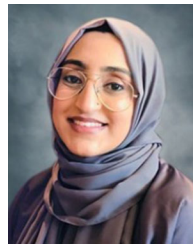
Madiha Farman received the B.Sc. and M.Sc. degrees in mechanical engineering from Khalifa University, Abu Dhabi, UAE, in 2017 and 2019, respectively.

Her research interests include CAD modeling, fabrication, and programming of experimental apparatus for soft robotics applications.

Marcello Calisti (Member, IEEE) received the B.Sc. degree in mechanical engineering from University of Perugia, Perugia, Italy, in 2005, the M.Sc. degree in biomedical engineering from University of Florence, Florence, Italy, in 2008 and the Ph.D. degree in biorobotics from Scuola Superiore Sant-Anna, Pisa, Italy, in 2012.

He is currently a Senior Lecturer in Agri-Roboticswith the Lincoln Institute for Agri-food Technology, University of Lincoln, Lincoln, U.K. He led or contributed to several national and international research projects. His research interests lie into the intersection of bioinspiration, soft, field and underwater robotics.
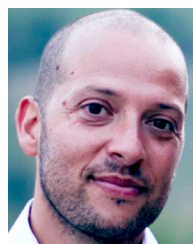
Francesco Giorgio-Serchi received the Laurea Degree (M.Sc. equivalent) in marine technologies from the University of Pisa, Pisa, Italy, in 2006, and the Ph.D. degree in computational fluid dynamics from the University of Leeds, Leeds, U.K., in 2011.

He is currently a Chancellor's Fellow (Lecturer) with the University of Edinburgh, Edinburgh, U.K., within the Institute of Integrated Micro and Nano Systems and the Edinburgh Centre for Robotics. Previously he was a Research Fellow with the University of Southampton, within the Fluid-Structure-Interaction group and prior to that he was with the Centre for Sea Technologies and Marine Robotics of the Scuola Superiore Sant-Anna, Pisa, Italy.

Cesare Stefanini (Member, IEEE) received the M.Sc. degree in mechanical engineering and the Ph.D. degree in microengineering, both with honors, from Scuola Superiore Sant-Anna (SSSA), Pisa, Italy, in 1997 and 2002, respectively.

He is currently a Professor with the BioRobotics Institute in the same University where he is the Head of the Creative Engineering Lab and also the Director of the Healthcare Engineering Innovation Center, Khalifa University, Abu Dhabi, UAE. His research activity is applied to different fields, including underwater robotics, bioinspired systems, biomechatronics, and micromechatronics for medical and industrial applications. He received international recognitions for the development of novel actuators for microrobots and he has been visiting Researcher with the University of Stanford, Center for Design Research.

Dr. Stefanini is the recipient of the "Intuitive Surgical Research Award." He is the author or coauthor of more than 160 articles on refereed international journals and on international conferences proceedings. He is the inventor of 15 international patents, nine of which industrially exploited by international companies. He is a member of the Academy of Scientists of the UAE and of the IEEE Societies RAS (Robotics and Automation) and EMBS (Engineering in Medicine and Biology).

Federico Renda (Associate Member, IEEE) received the B.Sc. and M.Sc. degrees in biomedical engineering from the University of Pisa, Pisa, Italy, in 2007 and 2009, respectively, and the Ph.D. degree in biorobotics from the Biorobotics Institute, Scuola Superiore Sant-Anna, Pisa, in 2014.

Since 2015, he has been a Postdoctoral Fellow with the Khalifa University Robotics Institute (KURI), Khalifa University, Abu Dhabi, UAE, where he currently serves as an Assistant Professor with the Department of Mechanical Engineering. His research interests include dynamic modeling and control of soft and continuum robots using principles of geometric mechanics.